Iterative reconstruction from under-sampled Computed Tomography data

Sotirios Magkos

Univ.-Diss.

zur Erlangung des akademisches Grades
“doctor rerum naturalium”
(Dr. rer. nat.)
in der Wissenschaftsdisziplin “Angewandte Physik”

eingereicht an der
Mathematisch-Naturwissenschaftlichen Fakultät
Institut für Physik und Astronomie
der Universität Potsdam
und
der Bundesanstalt für Materialforschung und -prüfung

Potsdam, Donnerstag 10. November 2022

Hauptbetreuer:	Prof. Dr. Giovanni Bruno
Betreuer:	Dr. Dominique Bernard
Gutachter:	Dr. Andreas Kupsch

Published online on the
Publication Server of the University of Potsdam:
https://doi.org/10.25932/publishup-57278
https://nbn-resolving.org/urn:nbn:de:kobv:517-opus4-572789

Acknowledgements

Throughout the years I have worked on this dissertation, I have received a great deal of support and assistance.

I would first like to thank my supervisors Prof. Dr Giovanni Bruno and Dr Andreas Kupsch for the daily guidance and support. Their expertise was invaluable in formulating the research questions and methodology. I will be forever grateful to them both for entrusting me with this project and for giving me my first opportunity in research.

I would like to acknowledge my host institute, the *Bundesanstalt für Materialforschung und -prüfung*, and all my colleagues in the Division 8.5. They welcomed me wholeheartedly and I could always count on them in my pursuit of knowledge and solutions. I would particularly like to single out Dietmar Meinel and the late Sergei Evsevleev, who provided me the experimental data that has been used for this dissertation.

My project is part of the MUMMERING Innovative Training Network and has received funding from the European Union's Horizon 2020 research and innovation programme under Marie Skłodowska-Curie Grant Agreement No. 765604. I would like to thank every single one of fellow early-stage researchers, as well as their supervisors and industrial partners. I was fortunate to attend alongside them numerous schools, workshops, and meetings that helped define my work.

Among the people that were involved in MUMMERING, I would particularly like to acknowledge Dr Dominique Bernard, who has served as the second supervisor of this dissertation, and his doctoral student at the *Institut de Chimie de la Matière Condensée de Bordeaux*, Abdellatif Saadaldin. Our collaboration and exchange of ideas was instrumental in discovering new paths and applications in my research.

Finally, I could not have completed this dissertation without the love of my family and friends in my native Greece. Their support assisted me through this testing period.

Abstract

In X-ray computed tomography (XCT), an X-ray beam of intensity I_0 is transmitted through an object and its attenuated intensity I is measured when it exits the object. The attenuation of the beam depends on the attenuation coefficients along its path. The attenuation coefficients provide information about the structure and composition of the object and can be determined through mathematical operations that are referred to as *reconstruction*.

The standard reconstruction algorithms are based on the *filtered backprojection* (FBP) of the measured data. While these algorithms are fast and relatively simple, they do not always succeed in computing a precise reconstruction, especially from under-sampled data.

Alternatively, an image or volume can be reconstructed by solving a system of linear equations. Typically, the system of equations is too large to be solved but its solution can be approximated by iterative methods, such as the *Simultaneous Iterative Reconstruction Technique* (SIRT) and the *Conjugate Gradient Least Squares* (CGLS).

This dissertation focuses on the development of a novel iterative algorithm, the *Direct Iterative Reconstruction of Computed Tomography Trajectories* (DIRECTT). After its reconstruction principle is explained, its performance is assessed for real parallel- and cone-beam CT (including under-sampled) data and compared to that of other established algorithms. Finally, it is demonstrated how the shape of the measured object can be modelled into DIRECTT to achieve even better reconstruction results.

Zusammenfassung

Bei der Röntgen-Computertomographie (XCT) wird ein Röntgenstrahl der Intensität I_0 durch ein Objekt gesendet und seine abgeschwächte Intensität I gemessen, wenn er das Objekt verlässt. Die Abschwächung des Strahls hängt von den Abschwächungskoeffizienten entlang seines Weges ab. Die Schwächungskoeffizienten liefern Informationen über die Struktur und Zusammensetzung des Objekts und können durch mathematische Operationen, die als *Rekonstruktion* bezeichnet werden, bestimmt werden.

Die Standard-Rekonstruktionsalgorithmen basieren auf der *gefilterten Rückprojektio*n (FBP) der Messdaten. Diese Algorithmen sind zwar schnell und relativ einfach, doch gelingt es ihnen nicht immer, eine präzise Rekonstruktion zu berechnen, vor allem bei unzureichend abgetasteten Daten.

Alternativ kann ein Bild oder ein Volumen auch durch die Lösung eines Systems linearer Gleichungen rekonstruiert werden. In der Regel ist das Gleichungssystem zu groß, um gelöst zu werden, aber seine Lösung kann durch iterative Methoden angenähert werden, wie die *Simultaneous Iterative Reconstruction Technique* (SIRT) und die *Conjugate Gradient Least Squares* (CGLS).

Im Mittelpunkt dieser Dissertation steht die Entwicklung eines neuartigen iterativen Algorithmus, des *Direct Iterative Reconstruction of Computed Tomography Trajectories* (DIRECTT). Nach der Erläuterung seines Rekonstruktionsprinzips wird seine Leistung für reale Parallel- und Kegelstrahl-CT-Daten (einschließlich unterabgetasteter Daten) bewertet und mit der Leistung anderer etablierter Algorithmen verglichen. Schließlich wird gezeigt, wie die Form des gemessenen Objekts in DIRECTT modelliert werden kann, um noch bessere Rekonstruktionsergebnisse zu erzielen.

Erklärung

Ich erkläre, dass die Arbeit bisher an keiner anderen Hochschule eingereicht worden ist sowie selbständig und ausschließlich mit den angegebenen Mitteln angefertigt wurde.

Sotirios Magkos

Contents

Introduction **1**

1 Tomographic reconstruction **3**
1.1 Basic principles 4
1.2 Parallel-beam image reconstruction 6
1.3 Three-dimensional image reconstruction 10
1.4 Iterative reconstruction 13

2 Direct Iterative Reconstruction of CT Trajectories **17**
2.1 The original idea of the algorithm 17
2.2 A novel approach to DIRECTT 18
2.2.1 Parallel-beam image reconstruction 19
2.2.2 Cone-beam image reconstruction 23
2.2.3 Software 25

3 Image quality metrics **27**
3.1 Full-reference metrics 27
3.1.1 Using the measured projections as reference 30
3.2 No-reference metrics 33

4 Reconstruction from parallel-beam tomography data **37**
4.1 Sample images 37
4.2 Results and discussion 39
4.2.1 Simulation of a missing-wedge measurement 39
4.2.2 Reconstruction of a sample with large aspect ratio . . 45

5 Reconstruction from cone-beam tomography data **49**
5.1 Sample images 49
5.2 Results and discussion 52
5.2.1 Full-width measurement 52
5.2.2 Region-of-interest measurement 61

Summary and outlook **65**

Bibliography 74

List of Figures

1.1 Example of a computed tomography scanner. 4
1.2 The projection $p(s)$ of the uniform disk on the detector s is the product of the chord length t and the density ρ. The projections of a complicated figure are different at a different view angle. 5
1.3 The representation of the projections on the $s - \theta$ plane is called a sinogram. 5
1.4 Projections of a single element inside an empty space; reconstruction of the single element by back-projection. 7
1.5 Illustration of the projection-slice theorem. 8
1.6 Demonstration of the filtered back-projection algorithm. . . . 9
1.7 Perpendicular cross sections through a three-dimensional phantom. 11
1.8 Projections of the phantom in Figure 1.7 from 0° and 90°. . . 11
1.9 The coordinate system for the cone-beam algorithm developed by Feldkamp, Davis and Kress. 12
1.10 The circular orbit does not satisfy Tuy's condition, but the circle-and-lines and the helix orbits do. 12
1.11 Reconstruction of the Defrise phantom by the FDK algorithm for different cone angles. 13
1.12 Example of problem with nine unknowns and nine measurements. 14
1.13 Schematic view of the iterative reconstruction process. 15
1.14 Gradient descent algorithms modify the image estimate by a small step size in the opposite direction of that indicated by the gradient of the objective function. 15

2.1 A uniform disc and its reconstruction by back-projection. The plotted profiles show that, moving away from its center, the reconstructed image deviates from the real image. 20
2.2 The different steps of the DIRECTT algorithm. 22

2.3 Vertical cross section through a three-dimensional phantom; simulated projection of the phantom; vertical cross section through the phantom as reconstructed by DIRECTT when it lies within the field of view fully and only partially. 23
2.4 Reconstruction of the three-dimensional phantom, which lay partially within the field of view, with the modified version of DIRECTT. 24

3.1 The original Shepp-Logan phantom and the result of its reconstruction by the DIRECTT algorithm; plotted profiles of the reference and the reconstructed image. 28
3.2 Absolute difference between the images in Figure 3.1. 29
3.3 The Shepp-Logan phantom, along with the images resulting from adding noise or a constant value to it. 30
3.4 The Pearson correlation coefficient between a set of projections and the forward projection of the volumes that were reconstructed from this set by different versions of the DIRECTT algorithm. 31
3.5 Reconstruction of the Shepp-Logan phantom by FBP and DIRECTT from projections over the angular range $[0°, 135°]$, and the respective Radon transforms of the reconstructed images over the complete 180°-range. 32
3.6 The Pearson correlation coefficient (PCC) between the projections of the Shepp-Logan phantom and the Radon transform of the two reconstructed images in Figure 3.5 over 180°. 33
3.7 Magnification of the image, from Figure 3.7, that was reconstructed by FBP. 34

4.1 Tomograms of two metal matrix composite plates of different compositions. 37
4.2 Mean attenuation of the X-ray beam as a function of the projection angle θ during the measurement of the invar grid. 38
4.3 Projections corresponding to a single horizontal slice of the metal matrix composite sample; residual projections of the same slice after 40 iterations of DIRECTT. 40
4.4 Histograms of the values in the sinograms of Figure 4.3 . . . 40
4.5 Reconstruction of a horizontal slice of the metal matrix composite sample from 3000 projection. 41
4.6 A 600×600 μm^2 region of interest around the centre of each image in Figure 4.5. 42
4.7 Reconstruction of a horizontal slice of the metal matrix composite sample from projections that simulated a missing-wedge measurement. 43

4.8 A 600×600 μm^2 region of interest around the centre of each image in Figure 4.7. . . . 44
4.9 Pearson correlation coefficient (PCC) as a function of the projection angle. . . . 45
4.10 Orthogonal views of the volume of the invar grid that was reconstructed by DIRECTT. . . . 46
4.11 Images from the reconstructed volumes of the grid. . . . 46
4.12 The measured projection of the grid at angle $\theta = 0$; the *structural similarity index metric* image between the measured projection and the corresponding Radon transform of each volume. . . . 47

5.1 Photograph of a computed tomography scanner, which was designed and is operated by BAM, with a concrete rod placed on the rotating table. . . . 50
5.2 Geometric representation of the measurements of the concrete rod. . . . 51
5.3 A projection of the concrete rod; absolute value of the derivative of the mean integral attenuation along the detector columns u; vertical cross section through the centre of the volume that the back-projection of the data results in; absolute value of the derivative of the attenuation coefficient along the positive part of axis z. . . . 53
5.4 Orthogonal cross sections through the concrete rod after the back-projections of the measured data and through the corresponding model M. . . . 54
5.5 Orthogonal cross sections through the reconstructed volume of the concrete rod. . . . 55
5.6 Profiles across the centre of each XY-slice of Figure 5.5. . . . 56
5.7 MSE and SSIM of each reconstructed volume of the concrete rod. . . . 57
5.8 Projections of the slice of the detector row that, during the measurement, was parallel to the source plane; reconstruction of the slice from the sinogram by FDK. . . . 59
5.9 Result of the back-projection of the sinogram in Figure 5.8 and model of the artefacts. . . . 60
5.10 Reconstruction of the slice of the concrete rod by DIRECTT in two different magnifications. . . . 60
5.11 Common cross sections through the volumes of the concrete rod that were reconstructed by FDK and DIRECTT from the region-of-interest projections. . . . 62
5.12 The ROI as reconstructed from the full-widht and the truncated projections. . . . 63

List of Tables

2.1 Comparison of the processing time required for the reconstruction of the 256^3 Shepp-Logan. 25

4.1 The contrast-to-noise ratio (CNR) and the entropy of each image in Figure 4.5. 41
4.2 The CNR and entropy of each image in Figure 4.7, and their mean squared error and structural similarity index metric in reference to the image in Figure 4.5 that was reconstructed by CGLS. 43
4.3 The contrast-to-noise ratio and entropy of each reconstructed volume, and the SSIM between the Radon transform of each volume and the measured projections. 48

5.1 The contrast-to-noise ratio and the entropy of each volume in Figure 5.5. 55
5.2 The MSE and the SSIM of the slices in Figures 5.8 and 5.10 in reference to the corresponding slice of the volumes in Figure 5.5 that were reconstructed by FDK and DIRECTT. 61
5.3 The MSE and SSIM of each volume in Figure 5.12 in reference to the volume in Figure 5.5 that was reconstructed by FDK. . 63

List of Published Manuscripts

1. S. Magkos, A. Kupsch, and G. Bruno. Direct Iterative Reconstruction of Computed Tomography Trajectories Reconstruction from limited number of projections with DIRECTT. *Review of Scientific Instruments*, 91(10):103107, 2020.

2. S. Magkos, A. Kupsch, and G. Bruno. Suppression of Cone-Beam Artefacts with Direct Iterative Reconstruction Computed Tomography Trajectories (DIRECTT). *Journal of Imaging*, 7(8):147, 2021.

Introduction

The project that resulted in this dissertation was one of the 15 projects that the Innovative Training Network MUMMERING [11] comprised. MUMMERING encompasses all aspects of tomography, including image reconstruction, which is the main subject of this work. More specifically, the dissertation focuses on the development and the performance of a novel reconstruction algorithm, the *Direct Iterative Reconstruction of Computed Tomography Trajectories* (DIRECTT).

This dissertation is split into five chapters:

Chapter 1 introduces the basic principles of tomographic reconstruction from parallel- and cone-beam data, as well as the iterative reconstruction algorithms.

Chapter 2 explains the original idea of DIRECTT and describes a novel approach that greatly increases its efficiency.

Chapter 3 is an overview of image quality metrics that can be used to assess the performance of the reconstruction algorithms.

Chapter 4 offers an assessment of DIRECTT and other established algorithms on the reconstruction from parallel-beam data. Further emphasis is given on cases of missing-wedge tomography.

Chapter 5 offers an assessment of the same algorithms on the reconstruction from cone-beam data. The chapter also demonstrates how artefacts can be modelled into DIRECTT to achieve higher reconstruction performance.

Chapter 1

Tomographic reconstruction

X-ray computed tomography is used to reconstruct cross-sectional images within a studied object by transmitting X-rays through it. X-ray photons can penetrate the object but not all photons that enter will be transmitted through it. Some photons interact with electrons, transfer part of their energy to them, causing them to recoil, and are scattered away. Other photons are absorbed by the object, converting their energy by mechanisms, such as the photoelectric effect. The X-ray intensity I_0 before entering the object and the intensity I after exiting the object are related according to the *Beer-Lambert law*:

$$I = I_0 e^{-p} \tag{1.1}$$

where p is the line integral of the linear attenuation coefficients μ along the path z of the X-rays. In case of uniform attenuation, Equation 1.1 becomes

$$I = I_0 e^{-\mu z}. \tag{1.2}$$

The attenuation coefficient is a property of the material, but it also depends on the energy of the radiation that penetrates the material.

An example of a CT scanner is shown in Figure 1.1. During the scan, an X-ray beam of intensity I_0 is generated by the source, which is highlighted by the red frame. The studied object is placed on a rotating table (orange frame) so that it can be irradiated by the beam from several, typically thousand, different views. A detector (yellow frame) measures the intensity I of the beam that exits the object in the form of a two dimensional (2D) image. According to Equation 1.1, the line integral of the attenuation coefficients is

$$p = \ln\left(\frac{I_0}{I}\right). \tag{1.3}$$

The structure and composition of the object can be subsequently determined based on these coefficients through mathematical operations [13]. This process is referred to as *reconstruction*

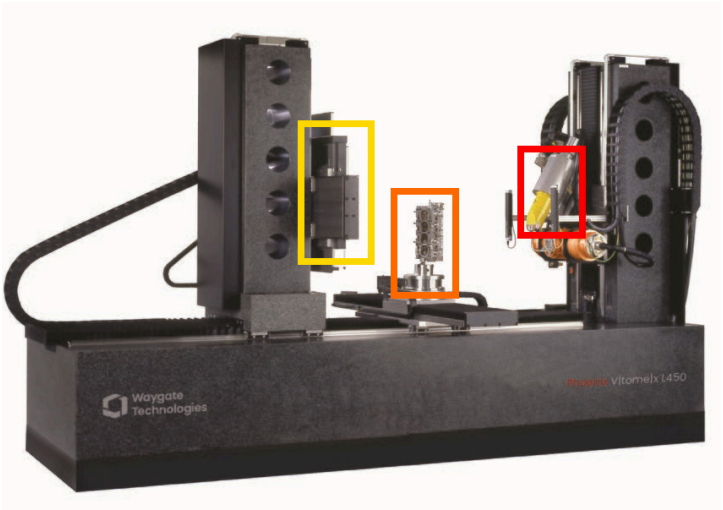

Figure 1.1: Example of a computed tomography scanner. The image is reproduced from Reference [54].

CT is a long-established method in the field of diagnostic medicine, where it enables the examination of patients' internal organs with high precision in a non-invasive manner. The revolutionary impact of the technique led to the 1979 *Nobel Prize in Physiology or Medicine* being awarded to **Allan MacLeod Cormack** and **Godfrey Hounsfield** "for the development of computer-assisted tomography" [44].

In the decades that followed the development of the first CT scanner by Hounsfield [24], the technique has also found applications outside of medicine, in the fields of materials analysis, non-destructive testing [16, 47], and metrology [26] among others. Examples of such applications include the detection of defects [20], the evaluation of porosity [30], and the determination of material and damage behaviour [49].

1.1 Basic principles

In tomography, *image reconstruction* refers to the process of producing a tomographic image from a set of projections. For the example of a uniform disk of density ρ, such as that of Figure 1.2a, its *projection* $p(s)$ on the detector s can be calculated as the product of the chord length t and the density ρ. It is therefore equivalent to the *line integral* [12]. Given the uniformity of the object, its projection would be the same regardless of the view angle. For the more complicated object of Figure 1.2b, projections from different angles are different from one another [7].

The calculation of the projections of an object is also known as the *Radon*

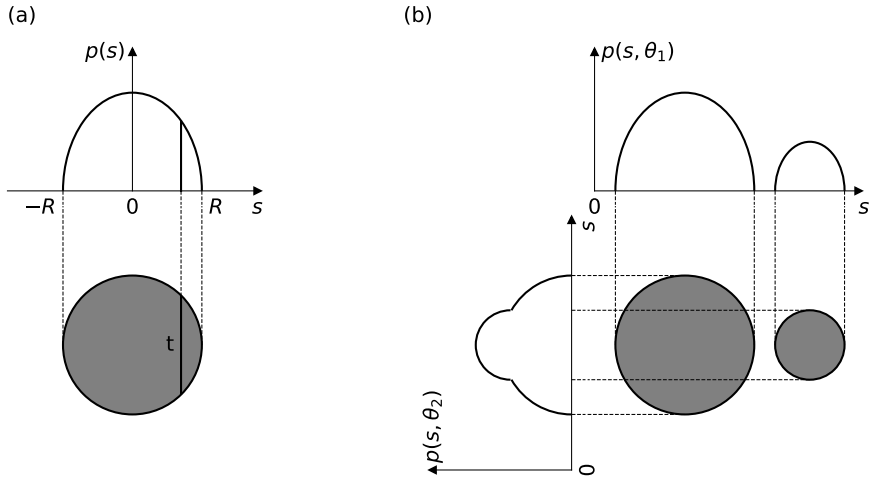

Figure 1.2: (a) The projection $p(s)$ of the uniform disk on the detector s is the product of the chord length t and the density ρ. (b) The projections of a complicated figure are different at a different view angle.

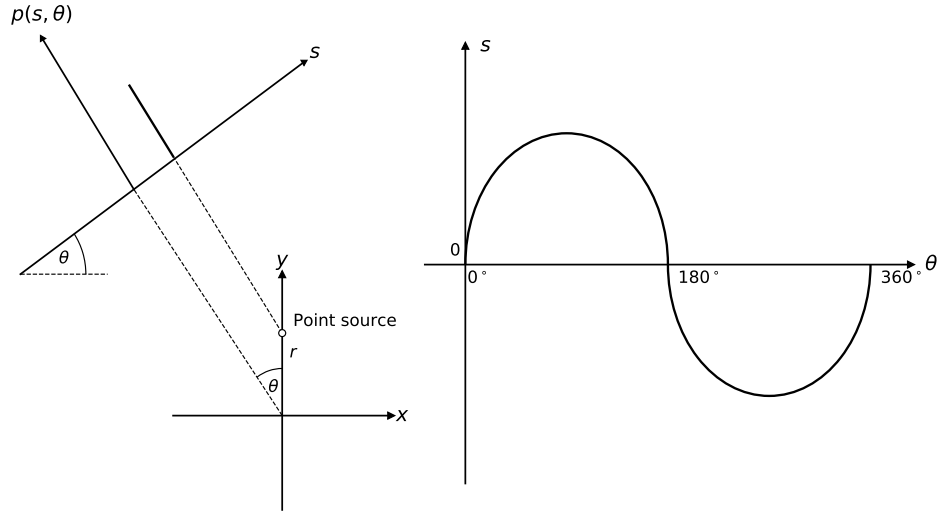

Figure 1.3: The representation of the projections on the $s-\theta$ plane is called a sinogram.

transform. More specifically, in an n-D space, the Radon transform of an n-D object is its $(n-1)$-D hyperplane integral.

The dependency of the projection to the angle θ can be better illustrated using the example of a point source on an $x-y$ coordinate system. Lines are drawn across the plane, orthogonal to a hypothetical one-dimensional detector, and the line integral is evaluated. Depending on whether the line touches the point source or not, the intensity registered by the detector at the end of the line is either one or zero (Figure 1.3a) [7]. If the locations of the intensity spikes were displayed in 2D in a common s-θ coordinate system, the resulting trajectory would resemble a sine wave (Figure 1.3c). For this reason, the full projection data set can be referred to as a *sinogram*.

1.2 Parallel-beam image reconstruction

While many modern CT systems use a cone-beam geometry, X-ray imaging beamlines at synchrotron radiation facilities use a geometry in which the beam can be considered parallel due to the large distance between the source and the measured object. It is instructive, therefore, to introduce the concepts that describe parallel-beam image reconstruction.

In Figure 1.4a, a single element inside an otherwise empty space is projected from different angles. The element can be reconstructed from this projection data by re-distributing the registered intensity back along the projection path, in a process referred to as *back-projection*. Not knowing where the element that resulted in the registered intensity is located, the intensity must be back-projected in equal amounts of the full value along the path (Figure 1.4b) [7]. However, compared to the original image, the back-projection from many different angles will result in a blurrier image and disproportionately higher values, due to the aforementioned superposition, where the element is.

This example of a single element is useful for demonstrating the concepts of *projection* and *back-projection*. Note, however, that two projections would be enough for its reconstruction.

A more precise reconstruction of the single element would require the dissolution of the overlapping effect through *filtering* of the projection data. The filtering can be implemented either as a multiplication in the Fourier domain or as a convolution in the spatial domain.

The foundation of the filtering process is the *projection-slice theorem*. In the 2D case, the theorem states that the one-dimensional (1D) Fourier transform $P(\omega)$ of the projection $p(s)$ on a line (i.e., a 1D detector) of a two-dimensional object is equal to a 1D slice through the origin of the 2D Fourier transform $F(\omega_x, \omega_y)$ of that object which is parallel to the line/detector [3, 53]. It is illustrated for the example of the Shepp-Logan phantom [51] in

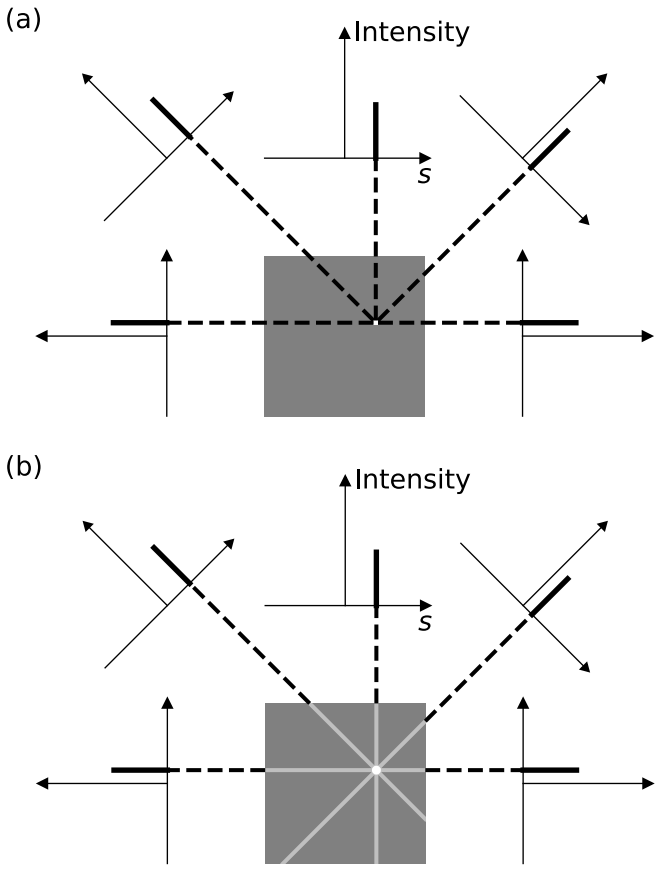

Figure 1.4: (a) Projections of a single element inside an empty space. (b) Reconstruction of the single element by back-projection.

Figure 1.5a. Expressed mathematically, the theorem is given as

$$P(\omega, \theta) = F(\omega \cos\theta, \omega \sin\theta). \tag{1.4}$$

It is deduced, from the theorem, that projections of the object acquired over at least 180° are equivalent to slices that cover the entire 2D Fourier space. When $F(\omega_x, \omega_y)$ is known, the measured object can be obtained by a 2D inverse Fourier transform (Figure 1.5b) [3, 53]. Including multiple 'central slices' results in a higher density in the central region of the Fourier space, which represents low frequencies. This non-uniform density in the Fourier space leads to the overweighting of low-frequency components and is the reason behind the blur of images produced by back-projection.

The above non-uniformity is proportional to $\frac{1}{\sqrt{\omega_x^2+\omega_y^2}}$. The standard way to compensate for it is to multiply the 1D Fourier Transform $P(\omega, \theta)$

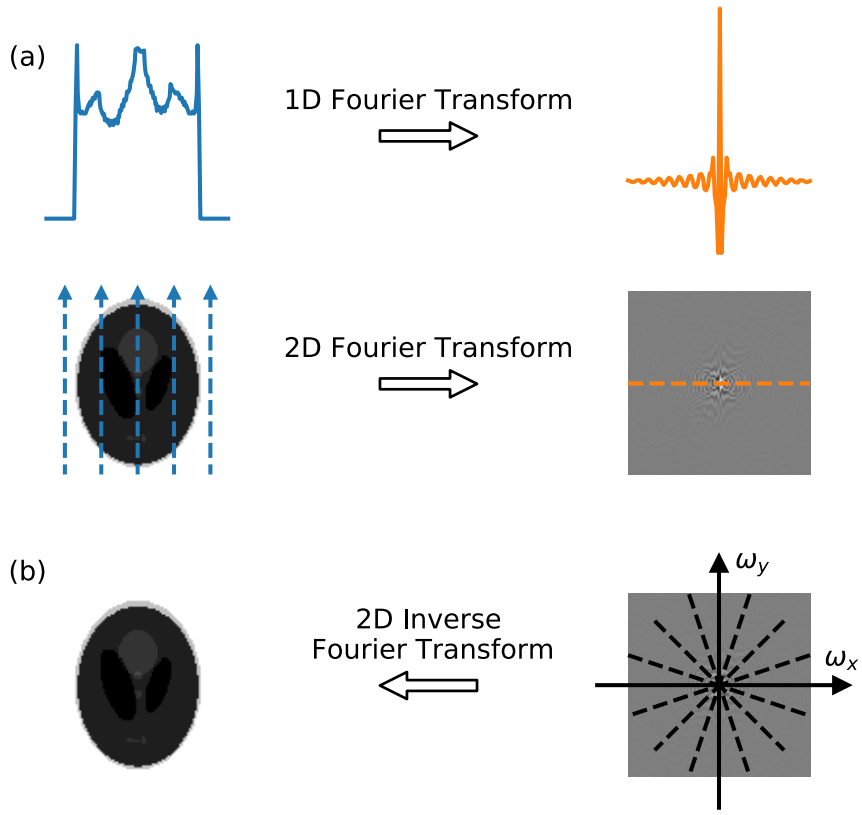

Figure 1.5: Illustration of the projection-slice theorem.

of the projection data by $H(\omega) = |\omega|$ and calculate the 1D inverse Fourier Transform of this product. If the filtered projection data $Q(\omega, \theta)$ are back-projected after this treatment, the exact image of the measured object is obtained. This method is referred to as the *filtered back-projection* (FBP) and the function $|\omega|$ is called *ramp filter*, after its appearance. The ramp filter is a high-pass filter, meaning that it suppresses the low-frequency components and enhances the high-frequency components.

Multiplication in one domain is the equivalent to convolution (denoted with the symbol $*$) in the other domain [62]. Given this property, the ramp-filtered data $q(s, \theta)$ of the projection $p(s, \theta)$ can also be obtained without using the Fourier transform at all:

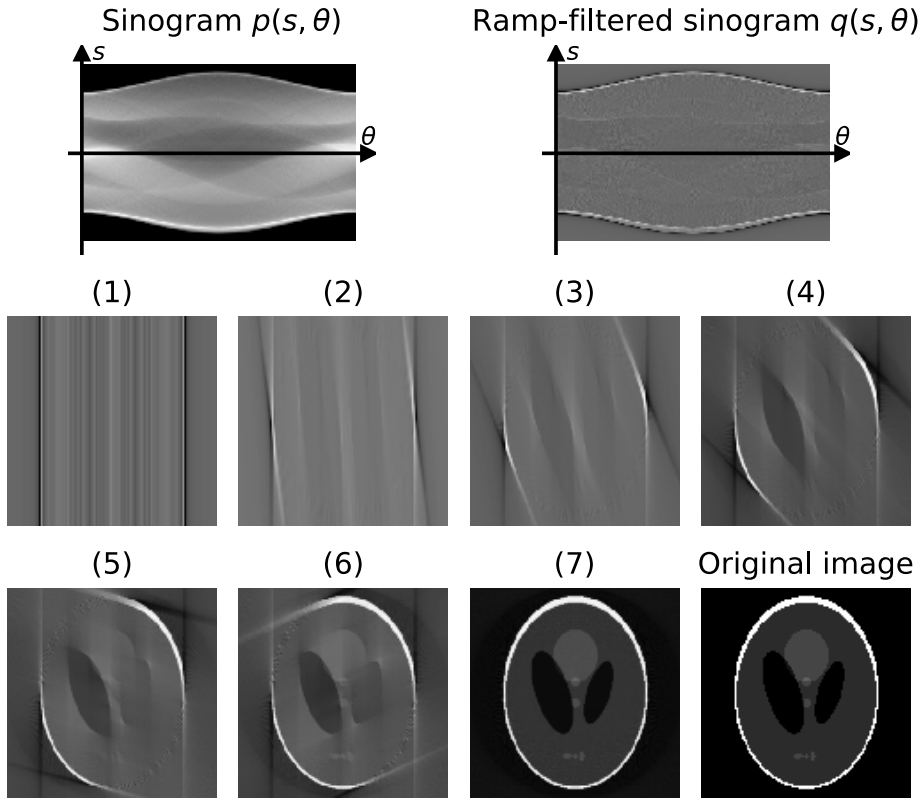

Figure 1.6: Demonstration of the filtered back-projection algorithm: The Radon transform $p(s,\theta)$ of the Shepp-Logan phantom (lower right corner) is computed and the ramp filter is applied to it. The filtered data $q(s,\theta)$ is back-projected along the projection path for all angles (images (2)-(7)) until the reconstructed image resembles the phantom.

	$Q(\omega)$	$=$	$P(\omega)$	$\times$	$H(\omega)$
1D Fourier transform pair	$\Updownarrow$		$\Updownarrow$		$\Updownarrow$
	$q(s)$	$=$	$p(s)$	$*$	$h(s)$

Instead, the 'Ramachandran-Lakshminarayanan' kernel, which is the inverse Fourier transform of the ramp filter, is employed. The continuous version of

the convolution kernel is

$$h(s) = \frac{1}{2}\frac{\sin(\pi s)}{\pi s} - \frac{1}{4}\left[\frac{\sin\left(\frac{\pi s}{2}\right)}{\frac{\pi s}{2}}\right]^2 \tag{1.5}$$

but, since the projection data are measured with a sampling interval of σ, the convolver needs only be known with the same sampling interval:

$$h(n\sigma) = \begin{cases} \frac{1}{4\sigma^2}, & n = 0 \\ 0, & n \text{ even} \\ \frac{-1}{n^2\pi^2\sigma^2}, & n \text{ odd.} \end{cases} \tag{1.6}$$

A demonstration of the FBP algorithm is given in Figure 1.6. The Shepp-Logan phantom is shown in the lower right corner. Its Radon transform $p(s,\theta)$ is computed and the ramp filter is applied to it, resulting to the visibly sharper $q(s,\theta)$ data. The image labelled (1) shows the back-projection of $q(s,\theta)$, which is nothing more that smearing back the filtered data along the projection path, for the first angle. In images (2)-(7), as data from more angles, up to the full 180°, are back-projected the reconstructed image is gradually shaped and finally closely resembles the original image [60].

1.3 Three-dimensional image reconstruction

Parallel-beam data The reconstruction of a 3D volume from parallel-beam data often can be decomposed into the reconstruction of individual 2D slices based on the rays that are confined within a trans-axial slice (detector row). When this is not applicable or desirable, the reconstruction can be based on the extension of the projection-slice theorem 3D.

In that case, the theorem states accordingly that the 2D Fourier transform $P(\omega_u, \omega_v, \vec{\theta})$ of the projection $p(u, v, \vec{\theta})$ of a 3D object is equal to a slice through the origin of the 3D Fourier transform of the object which is parallel to the detector. Here, $\vec{\theta} = (\sin\theta\cos\phi, \sin\theta\sin\phi, \cos\theta)$ is the normal direction of the $u - v$ plane. In polar coordinates, the theorem is expressed as

$$\begin{aligned} P(\omega_u, \omega_v, \vec{\theta}) =& F(-\omega_u \sin\phi - \omega_v \cos\theta\cos\phi, \omega_u \cos\phi \\ & - \omega_v \cos\theta \sin\phi, \omega_v \sin\theta) \end{aligned} \tag{1.7}$$

If the trajectory of $\vec{\theta}$ is a great circle (the intersection of a sphere and a plane that passes through the centre point of it), the measured $P(\omega_u, \omega_v, \vec{\theta})$ planes fill up the entire $(\omega_x, \omega_y, \omega_z)$ Fourier space. For the 3D reconstruction, in accordance to the 2D case, the projection $p(u, v, \theta)$ is filtered by a 2D filter. The back-projection of the filtered data $q(u, v, \theta)$ returns the reconstructed object.

Cone-beam data Two cross sections through a 3D phantom are shown in Figure 1.7. The projections of the phantom acquired in a cone-beam geometry from 0° and 90° are shown in Figure 1.8.

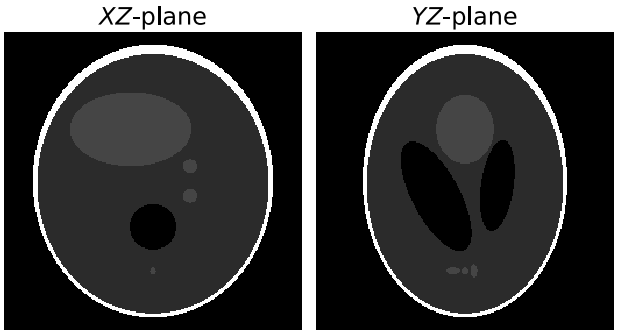

Figure 1.7: Perpendicular cross sections through a three-dimensional phantom.

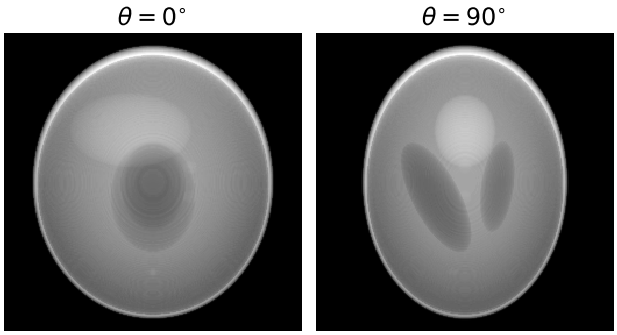

Figure 1.8: Projections of the phantom in Figure 1.7 from 0° and 90°.

The standard reconstruction algorithm for cone-beam data acquired from a circular focal-point trajectory was developed by Feldkamp, Davis and Kress (FDK) [14]. The coordinate system for FDK is shown in Figure 1.9. During the reconstruction, the projections are scaled by $\cos\alpha$, where α is the half-cone angle for each detector pixel. Each row is subsequently filtered with the ramp filter. Finally, the filtered data are back-projected towards the focal point, with the value of each point on the back-projection path (e.g. the red point on the red path of Figure 1.9) weighted proportionately to its distance to the focal point.

Tuy's condition states that every plane that intersects the measured object must contain a cone-beam focal point [55]. It is obvious from Figure 1.10a that the circular orbit does not satisfy the condition. As a consequence,

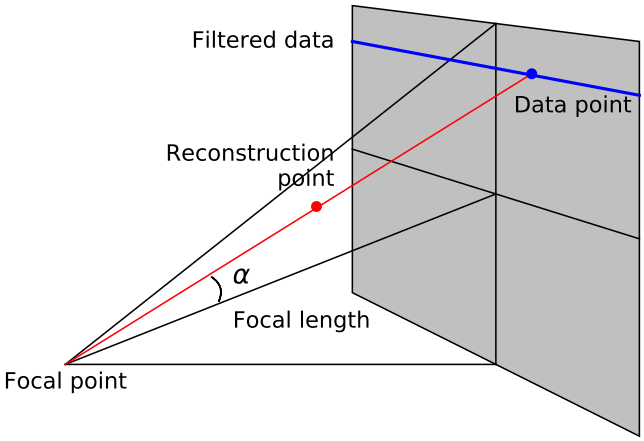

Figure 1.9: The coordinate system for the cone-beam algorithm developed by Feldkamp, Davis and Kress.

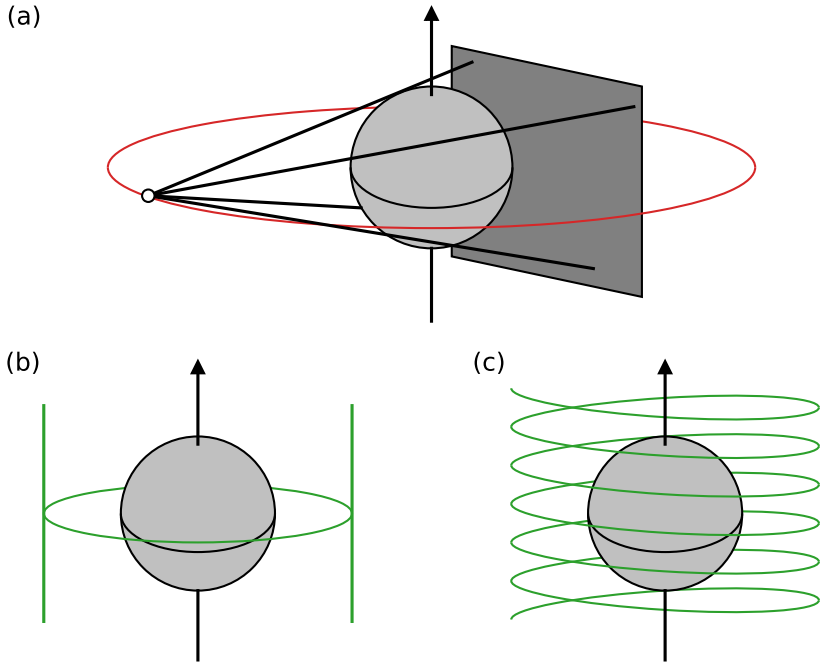

Figure 1.10: The circular orbit (a) does not satisfy Tuy's condition, but the circle-and-lines (b) and the helix (c) orbits do.

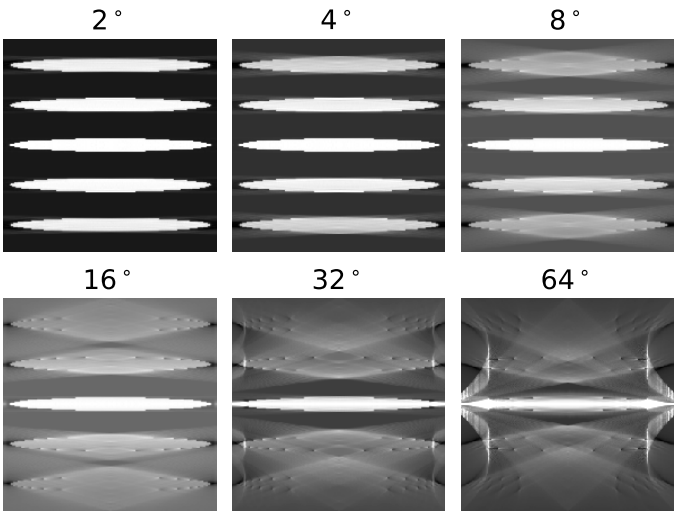

Figure 1.11: Reconstruction of the Defrise phantom [61] by the FDK algorithm for different cone angles.

FDK is exact at the orbit plane and performs sufficiently well away from it for small cone angles. For larger angles though, severe artefacts appear away from the orbit plane, as demonstrated in Figure 1.11 [61].

It is worth noting that there are projection geometries, other that the circular orbit, that do satisfy Tuy's condition. Such geometries are the circle-and-line orbit (1.10b) and the helical orbit (1.10c).

1.4 Iterative reconstruction

The image of Figure 1.12 is discretized into pixels (picture elements). It can be reconstructed by solving a system of linear equations [17]. These equations express the relation of the pixels of the image x_j and the projections p_i. They can be written in the matrix form as

$$AX = P \tag{1.8}$$

where $X = [x_1, x_2, ..., x_9]^T$, $P = [p_1, p_2, ..., p_9]^T$, and A is a matrix the elements a_{ij} of which represent the contribution of the pixel x_j to the projection p_i.

The reconstruction of the image in Figure 1.12 would require the solution of a system of only nine equations. In reality, a volume will consist of possibly millions, or even billions, of voxels and, accordingly, thousands of projections. Therefore, the corresponding system of equations will be too large to be solved. Iterative methods [15] can be used to find an approximate

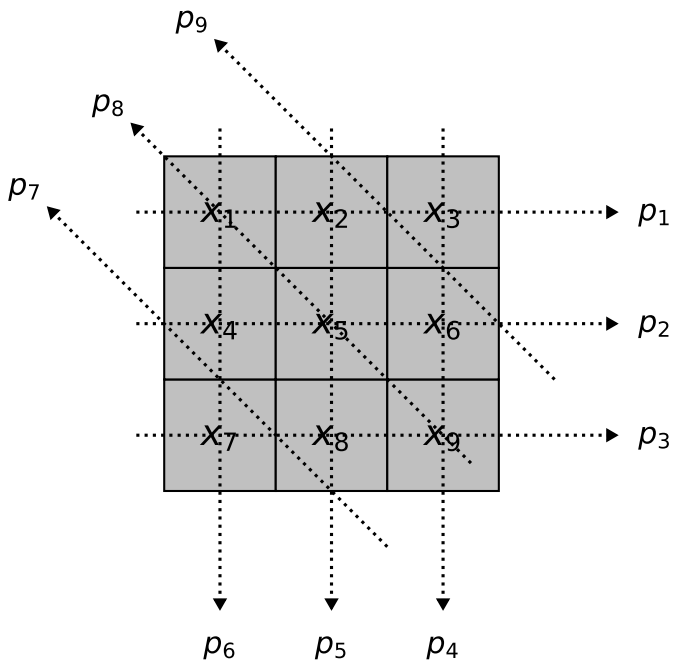

Figure 1.12: Example of problem with nine unknowns and nine measurements.

solution to Equation 1.8 by minimizing the objective function

$$\chi^2 = ||AX - P||^2. \tag{1.9}$$

During each iteration:

1. the image estimate is forward projected;
2. the projected data are compared to the measured data;
3. the discrepancies between the two are back-projected;
4. the back-projected data are used to modify the image estimate.

Figure 1.13 offers a schematic view of the iterative reconstruction process [5].

There are numerous iterative reconstruction algorithms. *Gradient descent* algorithms modify the image estimate by a small step size in the opposite direction of that indicated by the gradient of the objective function. The general form of the algorithm for the iteration k is

$$X^{k+1} = X^k - \alpha_k \vec{\Delta}_k, \tag{1.10}$$

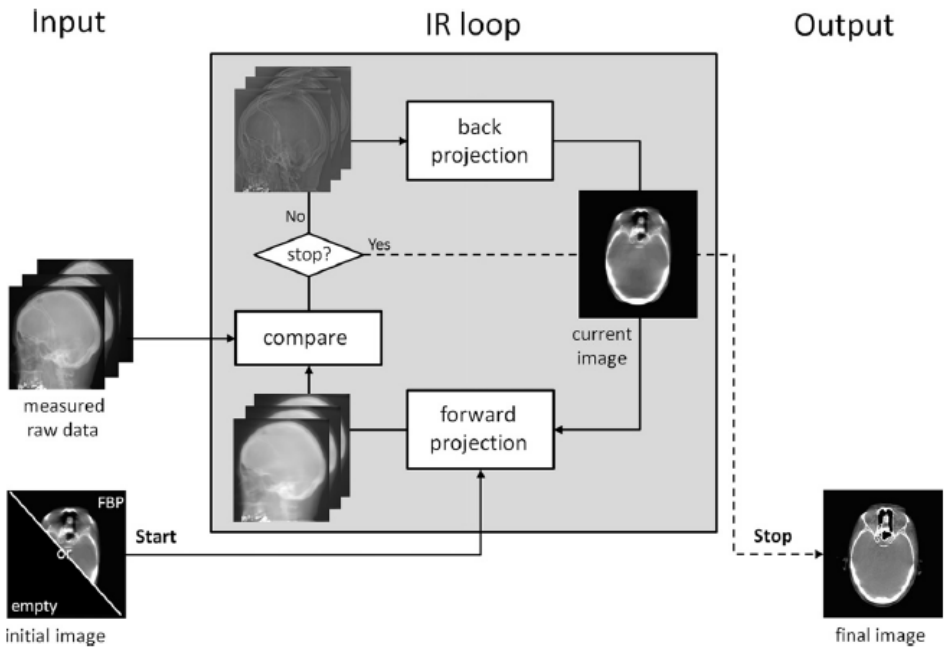

Figure 1.13: Schematic view of the iterative reconstruction process. The image was reproduced from Reference [5]

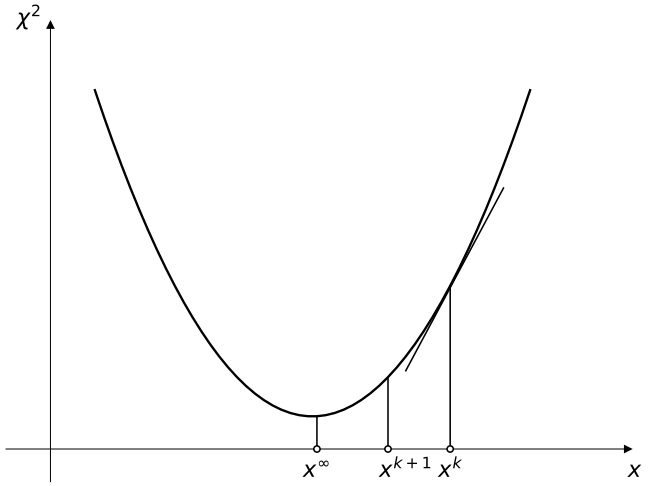

Figure 1.14: Gradient descent algorithms modify the image estimate by a small step size in the opposite direction of that indicated by the gradient of the objective function.

where α is the step size and $\vec{\Delta}$ is the gradient of the objective function. Specifically,

$$\vec{\Delta}_k = \nabla||AX - P||^2 = 2A^T(AX - P). \tag{1.11}$$

In the above relation, the product AX represents the Radon transform of image X, while multiplication by A^T represents the back-projection. In the example of Figure 1.14, the gradient of the objective function for the solution x^k of a pixels is positive. During its next iteration, the algorithm will move downwards towards an updated solution x^{k+1}.

Examples of variations of the gradient descent algorithms are the *Simultaneous Iterative Reconstruction Technique* (SIRT) [15, 19] and the *Conjugate Gradient Least Squares* (CGLS) [23] algorithms. SIRT is expressed algebraically as

$$X^{k+1} = X^k + \alpha C A^T R(P - AX^k). \tag{1.12}$$

C and R are diagonal matrices composed of the inverse row sums of A and the inverse column sums of A, respectively. SIRT converges for a step size $0 < \alpha < 2$. CGLS modifies the image by following the conjugate, instead of the gradient. It typically converges faster than SIRT.

Chapter 2

The Direct Iterative Reconstruction of Computed Tomography Trajectories algorithm

2.1 The original idea of the algorithm

The idea of the *Direct Iterative Reconstruction of Computed Tomography Trajectories* (DIRECTT) algorithm was first proposed by Lange, Hentschel, and Kupsch [31, 32, 33] as an alternative to FBP [36]. It selectively traced single sinusoidal trajectories from within the set of all possible trajectories by appropriate criteria, such as their angular averaged weight or contrast to adjacent trajectories, and computed their filtered inverse Radon transform, in an iterative procedure, to form the reconstruction array. The Radon transform of these elements was subsequently subtracted from the original measured data and the obtained residual sinogram was treated the same way in the next iteration steps, until a pre-selected criterion of convergence was reached [27].

The application of DIRECTT was centred around the precise projection of the reconstruction array. To achieve this precision, which is essential for enhanced spatial resolution, the actual size and shape of the reconstructed elements were also taken into consideration. This approach complemented the abandonment of the spatial filtering, thus overcoming certain serious restrictions associated with the FBP. One of these restrictions arises from Nyquist's theorem, which limits the achievable spatial resolution to twice the detector pixel size. Any projections that are acquired by exceeding the Nyquist rate (oversampling) have no effect on the outcome of the reconstruction. However, since Nyquist's theorem refers to the non-equidistant angular sampling but not the detector-pixel sampling, the developers of DI-

RECTT claimed that, by oversampling the trajectories, could be enhanced beyond the limit that the theorem predicts [27]. Further advantages include improved reconstructed images in the cases of limited-view projections, as well as region-of-interest measurements [33, 22].

DIRECTT was developed for application on parallel-, fan-[27], and cone-beam [34] geometries. For the latter case, it has been shown to reduce artefacts that are associated with the FDK algorithm, particularly far outside the source plane. Local smearing by focal spot size and real detector response were also integrated into DIRECTT to increase the reconstruction quality [29].

The performance of DIRECTT has been investigated for a number of applications. In one of these, it was used to mitigate typical reconstruction artefacts in missing-wedge CT [28]. Such artefacts appeared as elongations of reconstructed details around the symmetry centre of the projections. A two-fold approach combined elements from discrete tomography, which were used to determine the coarse shape of objects, with subsequent refinements by iterations without mass restrictions [28].

DIRECTT has also been applied to data acquired with techniques other than X-ray computed tomography. It has coped with aperture-smearing effects of neutron computed tomography and offered advantages over FBP and SIRT while dealing with the simultaneous occurrence of numerous restrictions inherent to electron tomography [35].

2.2 A novel approach to DIRECTT

Despite being a promising alternative to FBP-type algorithms, DIRECTT was not developed to its full potential. The available source code, written in the programming language C, was not easy to use and its extension to 3D geometries, and particularly cone-beam geometries, was incomplete.

Additionally, there were some problems regarding the implementation of the reconstruction principle. According to this principle, certain trajectories within the measured projections should be singled out, during each iteration, and subsequently only the values of the elements that corresponded to those trajectories would be updated. In practice, it was easier to reconstruct the volume by FBP, discard the elements with values lower than a threshold value, which the user selected, and update the values of the remaining elements based on their individual projection (trajectory).

The use of FBP during each iteration required the convolution of the projections with a filter function, a much more computationally expensive operation than the simple back-projection. Apart from the computational cost, the constant filtering also resulted in the presence of salt-and-pepper noise in the reconstructed images. While noise is set to increase with a large number of iterations, filtering accelerates this effect. The added salt-and-

pepper noise required additional special filters for its suppression.

The efficiency of the algorithm was also potentially affected by the arbitrary selection of the threshold value that specified which reconstruction elements would be updated during each iteration. A threshold value that was either too high or too low could have a considerable impact on the reconstruction routine in terms of quality and time.

In this work, the idea of DIRECTT has been thoroughly revisited. By combining the existing principles with simple physical and mathematical concepts, as well as sophisticated software, an efficient, easy-to-use algorithm has been developed as a viable alternative to the standard reconstruction techniques.

2.2.1 Parallel-beam image reconstruction

Obviously, the only way to rid the algorithm of the computational cost of the FBP is to skip the filtering and simply back-project the measured data. Modifying this aspect of the algorithm will also affect the selection of the reconstruction-array pixels the values of which will be updated during each iteration.

The new approach for the selection of the pixels can be demonstrated for the simple example of a disc of $\mu = 1$ (Figure 2.1a, μ has dimensions of reciprocal length [L^{-1}]). The back-projection of the sinogram of the disc results in a blurry reconstruction (Figure 2.1a). The plot of the profiles through the centre of the disc and its reconstruction demonstrates how the two images differ from one another anywhere but their centres. Based on this observation and the reconstruction principle of DIRECTT, as it has been explained in this chapter, the threshold value for the initial iteration of the algorithm would be set to 1, and the central pixel of the reconstruction array would be updated.

In reality, the measured object typically will not be uniform. However, as long as its shape is known, the Radon transform of a virtual, uniform object C of the same shape and $\mu = 1$ can easily be computed. The relation between the threshold values for the initial iterations of DIRECTT for the real and virtual objects will be the same as the relation between the norm of each Radon transform. And since, following the same reasoning as for the disc of Figure 2.1, the threshold for C would be 1, the threshold for the real object will be

$$\beta_1 = \frac{||P||}{||AC||}, \tag{2.1}$$

where $||P||$ is the norm of the measured projections, and $||AC||$ is the norm of the computed projections of the object C. While a high precision in replicating the shape of the measured object in a virtual object is advantageous,

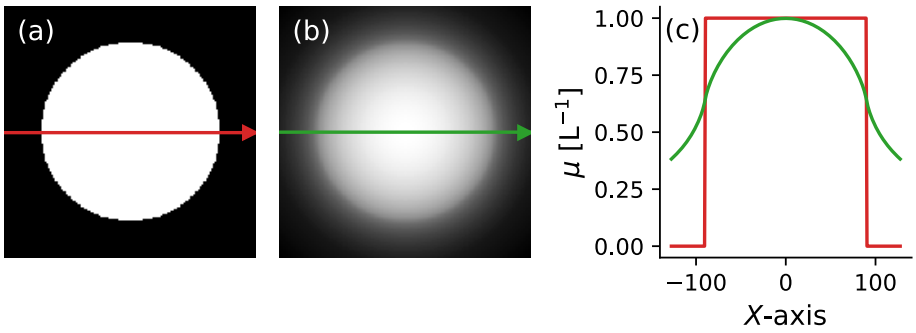

Figure 2.1: (a) A uniform disc of $\mu = 1$ (in units of reciprocal length $[L^{-1}]$). (b) The same disc as reconstructed by back-projection. (c) The plotted profiles show that, moving away from its center, the reconstructed image deviates from the real image.

it will rarely be achieved. The optimal approach, in this case, is to define C as a cylinder that is inscribed in the reconstruction volume.

Following the above modifications, DIRECTT can be expressed in a way that is compatible with Equations 1.8, 1.10, and 1.11:

$$X^{k+1} = X^k + \alpha \cdot \max\left(A^T(P - AX^k) - \beta_k J_{m,n,p}, 0\right). \tag{2.2}$$

The above expression describes the following steps:

1. Each iteration begins with the back-projection (A^T) of the residual projections over the $m \times n \times p$ reconstruction volume. The residual projections refer to the result of subtracting the Radon transform (A) of the partially reconstructed image (X^k) from the measured data (P).

2. A uniform matrix $\beta_k J_{m,n,p}$ is subtracted from the volume that results from the back-projection. $J_{m,n,p}$ is a matrix of ones of the same size as the reconstruction volume. The value of β_k depends on the state of the residual projections and thus decreases following each iteration:

$$\beta_k = \frac{||P - AX^k||}{||AC||}. \tag{2.3}$$

   The Radon transform of C is computed once, when β_1 is calculated. Therefore, its contribution to the total computational cost of the algorithm is minimal.

3. After the subtraction of $\beta_k J_{m,n,p}$, the negative values are truncated to zero. The result is a sparse matrix.

4. The sparse matrix is multiplied by an appropriate weight $\alpha \geq 1$ and is added to X^k. The value of α should be low enough that the reconstructed attenuation coefficients will not be irreversibly overestimated and, at the same time, high enough that the update of the array will not be incremental. In many of the cases that are presented in this thesis, α is set, during the first iteration of DIRECTT, so that it elevates the highest values of the sparse matrix to the level of β_1.

Following the last step, the Radon transform of the updated solution X^{k+1} is compared to P and all steps are repeated for the new set of residual projections. The algorithm is terminated after a certain number of iterations or when a pre-defined criterion is met. The criterion will be tied to a certain quality of the residual, such as the norm of the shape of its histogram.

The different steps of DIRECTT are demonstrated in Figure 2.2 using the projections of the Shepp-Logan phantom. During the first iteration of the algorithm (first row of the figure), the values of the sinogram are back-projected and β_1, calculated according to Equation 2.3, is subtracted from all pixels of the resulting image. After the subtraction, the values of the positive pixels are multiplied by α and are added to the reconstruction array to form the first estimate X_1. This estimate is forward projected so that its Radon transform can be subtracted from the original projections. The same steps are repeated for the residual projections.

Several iterations later (second row of Figure 2.2), the greyscale values of the residual projections are lower but the projections still resemble the original data. The attenuation coefficient values in the image after the back-projection of the residual data are also lower. Compared to the first iteration, more pixels of this smoother image are selected to be added to the reconstruction array, which already clearly resembles the phantom. Similarly, the Radon transform of the reconstruction array resembles the original data.

After more iterations (third row of Figure 2.2), most elements in the residual projections have greyscale values around zero. Even though the back-projection reveals some structure, the attenuation coefficient values of most pixels are too low to modify the reconstruction array significantly. Only fine details are updated, which leads to the termination of the algorithm. Different greyscale ranges have been used in each row of Figure 2.2, as is evident from the colour bars.

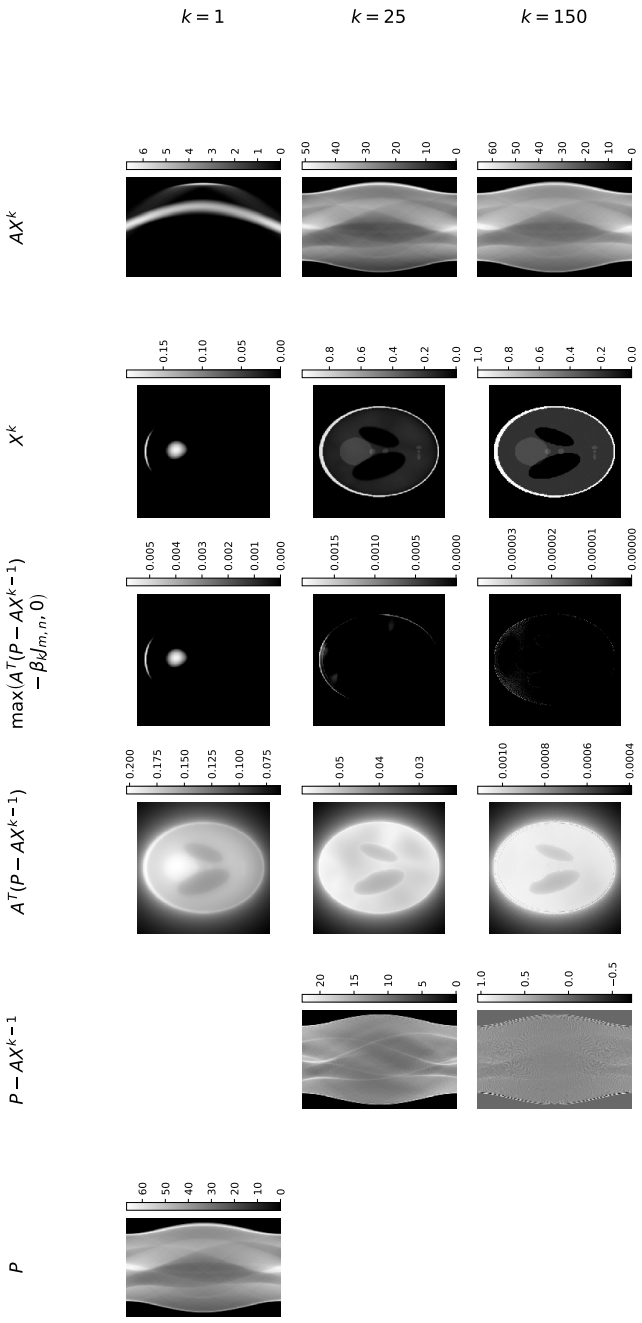

Figure 2.2: The different steps of the DIRECTT algorithm. Different greyscale ranges have been used in each row, as is evident from the colour bars.

2.2.2 Cone-beam image reconstruction

DIRECTT, as described above for the parallel-beam geometry, can also be implemented for the reconstruction from fan-beam projections. However, the algorithm does not always succeed in computing the reconstruction from cone-beam projections, specifically for large cone angles.

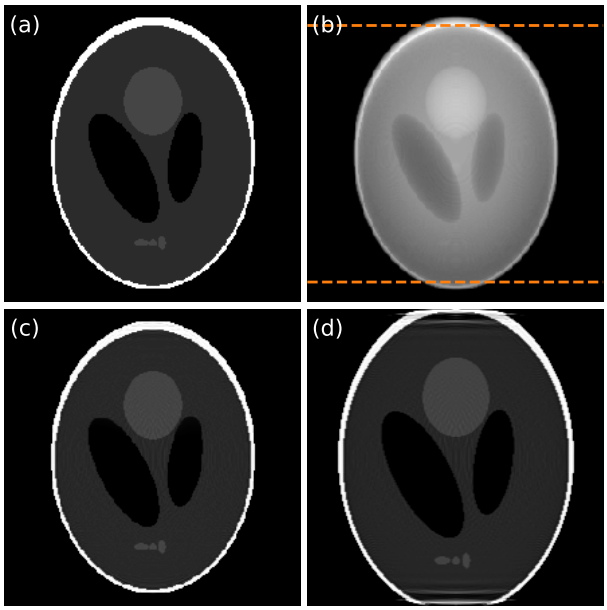

Figure 2.3: (a) Vertical cross section through a three-dimensional phantom. (b) Simulated projection of the phantom. The dashed lines indicate the extent of a shorter detector. (c-d) Vertical cross section through the phantom as reconstructed by DIRECTT when it lies within the field of view (c) fully and (d) only partially.

How the reconstruction can be affected by the projection geometry is demonstrated in Figure 2.3. The projection of a 3D phantom (vertical cross section shown in Figure 2.3a) is simulated for two detectors of different heights but of equal pixel spacing. A projection is shown in Figure 2.3b where the dashed lines indicate the height of the shorter detector. When the whole phantom lies within the field of view (FoV), DIRECTT reconstructs it accurately (Figure 2.3c). However, when the phantom is only partially within the FoV, severe artefacts arise in the reconstructed volume along the axial direction (Figure 2.3d). These artefacts arise largely because of a decrease, along that same direction, of the greyscale values that represent μ within the volume that the back-projection of the data results in [39]. If this decrease, and hence the associated artefacts, can be predicted for

Figure 2.4: Reconstruction of the three-dimensional phantom, which lay partially within the field of view, with the modified version of DIRECTT.

the given projection geometry, the volume can be corrected prior to the implementation of the subsequent steps of DIRECTT [39].

The artefacts can be indeed closely estimated by computing the Radon transform AC of a uniform object C, and subsequently back-projecting the result of the transform (A^TAC). The outcome of these successive operations is a volume $M = A^TAC$ that functions as a model of the distribution of greyscale values in AP. The latter is the volume that the back-projection of the measured data results in. After AP is divided by M pixel-by-pixel (Hadamard division [46]), DIRECTT can be successfully applied on the whole volume. M needs to be computed only once but is used during each iteration, meaning that the computational cost of the modification is small [39]. For cone-beam data, the expression of Equation 2.2 is adjusted to

$$X^{k+1} = X^k + \alpha \cdot \max\left(A^T(P - AX^k) \oslash M - \beta_k J_{m,n,p}, 0\right). \tag{2.4}$$

The symbol $\oslash$ denotes the Hadamard division[1].

Regarding the shape of the virtual object C, what was mentioned in the previous section in reference to the calculation of the value β_k (Equation 2.3) also applies here. The shape of C would ideally match the shape of the object that is being reconstructed. If this cannot be accurately estimated, the best approximation for C is a cylinder that is inscribed in the reconstruction volume.

Using the model M to correct the volume during each iteration of the DIRECTT algorithm for the case of the shorter detector of Figure 2.3 results in the reconstructed volume of Figure 2.4. Compared to Figure 2.3d, the artefacts in the axial direction are suppressed.

[1] $C_{ijk} = (A \oslash B)_{ijk} = \frac{A_{ijk}}{B_{ijk}}$. The operation is defined only if the matrices are of equal dimensions

2.2.3 Software

The reconstruction of all samples that are discussed in the dissertation was performed using a dedicated graphical user interface (GUI) [37]. The GUI was developed using the Python programming language and the Tkinter interface, and it incorporates the open-source ASTRA (All-Scales Tomographic Reconstruction Antwerp) toolbox [56]. Several algorithms, including the FBP, the FDK, the SIRT, and the CGLS, are available in the toolbox and can run with little input from the user. Regarding the implementation of DIRECTT, the operations of the forward- and back-projection were also performed via ASTRA. Using ASTRA, these two operations, which may be too computationally demanding for the central processing unit (CPU), can be offloaded on a graphics processor unit (GPU) using the CUDA (Compute Unified Device Architecture) platform.

The average processing times required for the reconstruction of the 256^3 Shepp-Logan phantom (64 MB) by FDK, and for a 100 iterations by each of SIRT, CGLS, and DIRECTT are listed in Table 2.1. All algorithms were executed on a computer equipped with an Intel i9-7900X CPU and an NVIDIA GeForce GTX 1080 Ti GPU. While DIRECTT appears to be slower than the other two iterative algorithms, these values cannot be compared on one-to-one basis given that SIRT and CGLS are *built into* the ASTRA toolbox, while DIRECTT is *built around* it. Finally, it is worth noting that the processing time required for the original version of DIRECTT [33, 35, 28] was approximately 20 times higher.

Table 2.1: Comparison of the processing time required for the reconstruction of the 256^3 Shepp-Logan phantom by FDK, and for 100 iterations of each of SIRT, CGLS, and DIRECTT on the same dataset.

Algorithm	Avg. processing time (s)	
FDK	8.39	(11)
SIRT	16.214	(41)
CGLS	28.09	(16)
DIRECTT	37.82	(90)

Chapter 3

Image quality metrics

Several reconstruction algorithms were discussed in Chapter 1. The development of another algorithm, such as DIRECTT, the principle and implementation of which were presented in Chapter 2, is only meaningful provided it can be shown that it outperforms the other algorithms in, at least, some aspects. It is, therefore, essential that the quality of the images that are reconstructed by each algorithm can be assessed using common metrics, so that all algorithms can be directly compared to one another. This chapter will discuss several such metrics that are classified into two major categories: full-reference and no-reference metrics.

3.1 Full-reference metrics

As their name suggests, *full-reference* quality metrics are used to assess the performance of a reconstruction algorithm based on how well the reconstructed image compares to a reference image. Ideally, this reference image corresponds to the *ground truth*. However, the ground truth is typically not known unless it is a phantom, i.e. a synthetic ideal structure, that has been measured.

In certain cases, full-reference metrics can still be used even if the ground truth is not known. Consider, for instance, that a sample was scanned under near-ideal conditions and with the appropriate sampling rate. In this case, the FBP will reconstruct a nearly optimal image. If the same sample were measured again under worse conditions (partial rotation, few projections) or such conditions were simulated for the original dataset, the image that had been earlier reconstructed by FBP could serve now as the reference by which the reconstruction of the new/simulated dataset would be assessed.

One of the simplest ways to compare an image to a reference is shown in Figure 3.1, where a *profile* of the Shepp-Logan phantom and the corresponding profile of the image as reconstructed by the DIRECTT algorithm are plotted. The plot shows that the reconstructed image is in excellent

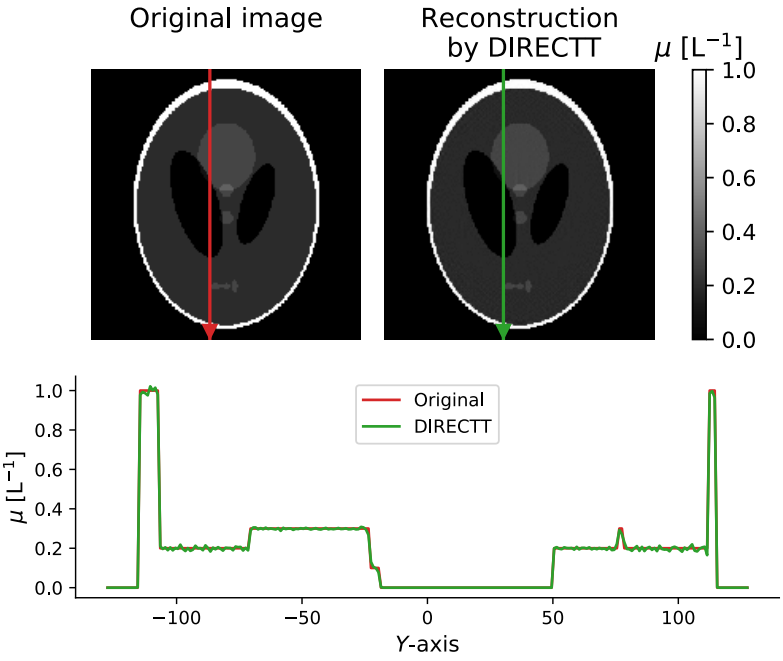

Figure 3.1: Top: The original Shepp-Logan phantom and the result of its reconstruction by the DIRECTT algorithm. The greyscale values represent the absorption coefficient μ (dimension of inverse length, L^{-1}) but no specific unit is assigned to them. Bottom: Plotted profiles of the reference and the reconstructed image. The two profiles practically coincide.

agreement with the actual phantom and that it contains very little noise.

The absolute difference between the two images of Figure 3.1 is shown in Figure 3.2. The image confirms the agreement between the original phantom and the reconstruction and reveals the sharpness of the edges as their main difference.

While useful conclusions can be extracted from Figures 3.1 and 3.2, it is more practical if the difference between the reconstructed image and the reference is quantified in a single value. A simple way to do this is through the calculation of the *mean squared error* (MSE) [58]. If x is the reference image and y is the reconstructed image, the MSE between the two is computed as

$$\mathrm{MSE}(x, y) = \frac{1}{n} \sum_{i=1}^{n} (x_i - y_i)^2 \,, \tag{3.1}$$

where n is the number of pixels, and x_i and y_i are the pixels indexed with i. If the two images are identical, the error between them will equal zero.

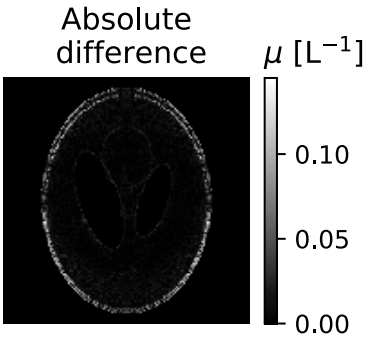

Figure 3.2: Absolute difference between the images in Figure 3.1.

The lower the value of MSE is, the more accurate the reconstruction is. For the image in Figure 3.1 that was reconstructed by DIRECTT, the MSE is 3.2×10^{-3}.

Despite its popularity, the MSE may not always be a reasonable fidelity measure. Take, for example, the images in Figure 3.3. The Shepp-Logan phantom (Figure 3.3, left) has greyscale values in the range [0,1]. Adding randomly distributed values of ± 0.2 results in a noisy image (Figure 3.3, middle). On the other hand, adding a constant value of 0.2 evenly to the original results in a brighter, but qualitatively similar image (Figure 3.3, right). Nevertheless, the MSE between either manipulated image and the original is 0.04, a result that reveals how the metric fails to predict human perception of image fidelity and quality [58].

The *Structural Similarity Index Metric* (SSIM) [59] is a metric that can be used instead of the MSE and potentially succeed where MSE fails. The compact form of its formula is

$$\mathrm{SSIM}(x, y) = l(x, y)^{\alpha} \cdot c(x, y)^{\beta} \cdot s(x, y)^{\gamma}. \tag{3.2}$$

The component functions represent comparison measurements between a reference image x and a reconstructed image y in terms of *luminance* (l), *contrast* (c), and *structure* (s). The individual functions are

$$l(x, y) = \frac{2\overline{x}\overline{y} + C_1}{\overline{x}^2 + \overline{y}^2 + C_1}, \tag{3.3}$$

$$c(x, y) = \frac{2\sigma_x \sigma_y + C_2}{\sigma_x^2 + \sigma_y^2 + C_2}, \tag{3.4}$$

and

$$s(x, y) = \frac{\sigma_{xy} + C_3}{\sigma_x \sigma_y + C_3}. \tag{3.5}$$

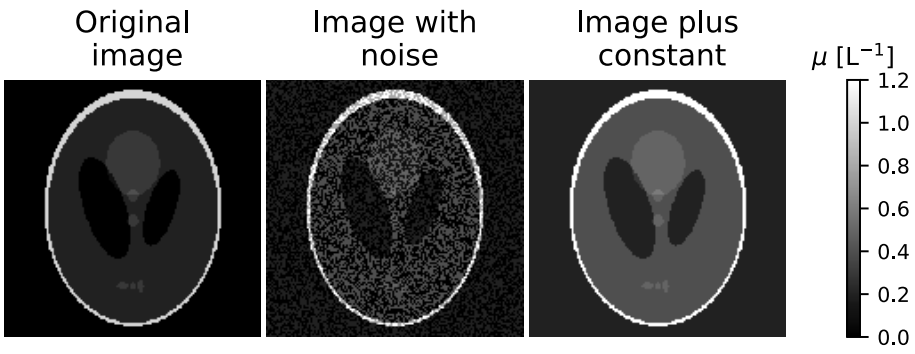

Figure 3.3: The Shepp-Logan phantom, along with the images resulting from adding noise or a constant value to it. Despite their obvious difference in quality, the mean squared error between either of the resulting images and the original is the same.

In the above equations, $\overline{x}$ and $\overline{y}$ are the mean of x and y, σ_x^2 and σ_y^2 are their variance, and $\sigma_{xy} = \frac{1}{n^2}\sum_i \sum_{j>i}(x_i - x_j)(y_i - y_j)$ is their covariance. The constants $C_1 = (K_1 L)^2$ and $C_2 = 2C_3 = (K_2 L)^2$ are included to avoid weak denominators in the respective equations. L represents the dynamic range of the pixel values, e.g. 255 for 8-bit images, and K_1, K_2 are small constants with default values of 0.01 and 0.03, respectively. The default value of each one of the weights α, β, and γ is 1. The SSIM has a value range of [0,1], with the optimal value being 1.

Going back to Figure 3.3, the SSIM is 0.16 for the noisy image and 0.4 for the image after adding a constant value. While neither index value is very high, the image that would be objectively perceived as more faithful to the original scores higher according to the metric. The SSIM for the image in Figure 3.1 that was reconstructed by DIRECTT is 0.96.

3.1.1 Using the measured projections as reference

As stated earlier, unless the scanned object is a phantom, there is no available reference to compare the reconstructed images to. What is available though is the acquired projections. It was discussed in Chapter 1 how certain iterative reconstruction algorithms, during their k-th iteration, adjust the image estimate X^{k-1} by a factor that is proportional to $||AX^k - P||$. This residual norm is essentially a quality metric and can also be used to assess the performance of the algorithm after its termination.

The norm of the projections difference is a global metric. Instead, $P(u, v, \theta)$ and $(AX)(u, v, \theta)$ can be compared using local metrics. An example of a local metric is the correlation coefficient. Their correlation may

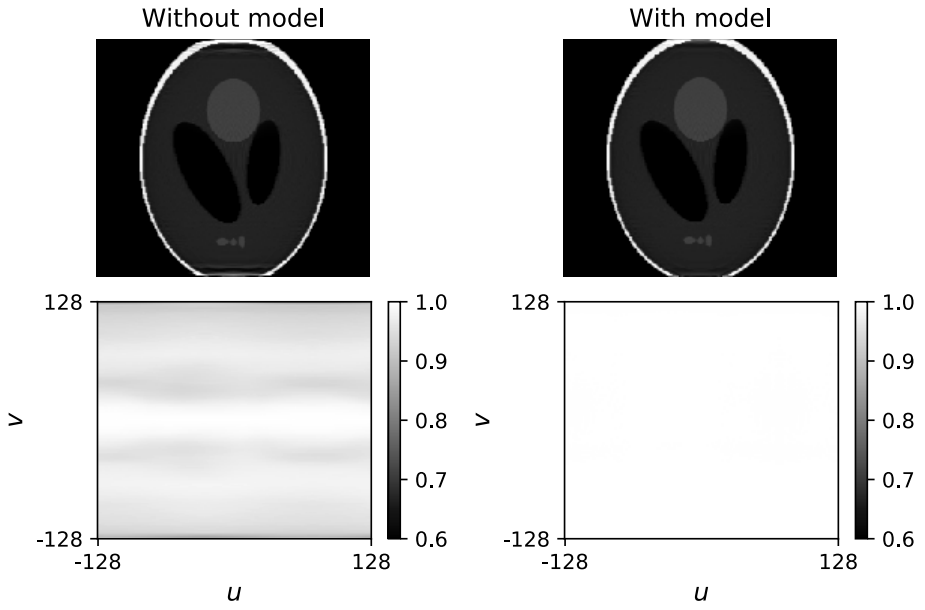

Figure 3.4: The Pearson correlation coefficient between a set of projections and the forward projection of the volumes that were reconstructed from this set by different versions of the DIRECTT algorithm.

be calculated over all projection angles θ as a function of the coordinates (u, v) (detector pixels). Alternatively, it may be calculated for individual cross sections as a function of θ.

The cross sections from Figures 2.3d and 2.4 are reproduced in Figure 3.4. Below either cross section, the *Pearson correlation coefficient* (PCC) [48] between the forward projection of the corresponding volume and the projections from which the volume was reconstructed (2.3b, between the dashed lines) is plotted for each detector pixel. For samples $x = \{x_1, x_2, ..., x_n\}$ and $y = \{y_1, y_2, ..., y_n\}$, the PCC is computed according to the formula

$$r_{x,y} = \frac{\sigma_{xy}}{\sigma_x \sigma_y} \tag{3.6}$$

where σ_x and σ_y the standard deviation of each sample and σ_{xy} their covariance. The PCC always has values between 1 and -1, ranging from total correlation to total anti-correlation.

The reader is reminded that the volume (a cross section of which is shown) in Figure 2.3d was reconstructed by the original version of DIRECTT, while the volume in Figure 2.4 was reconstructed by DIRECTT following its correction by a model M, as defined in Equation 2.4. When the model M is not incorporated into DIRECTT, the calculated PCC increases immediately over and below the source plane, but decreases fast away from

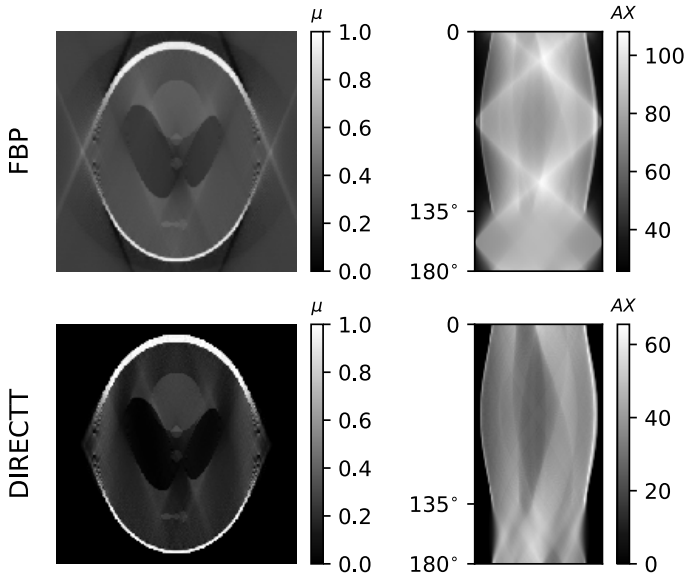

Figure 3.5: Reconstruction of the Shepp-Logan phantom by FBP and DIRECTT from projections over the angular range $[0°, 135°]$, and the respective Radon transforms of the reconstructed images over the complete 180°-range.

it, as it would be expected by observing the artefacts that are visible in Figure 2.3d. When the model M is incorporated into the algorithm, the calculated PCC is near 1 for every detector pixel.

The PCC can also be calculated as a function of the projection angle. The reconstruction of the 2D Shepp-Logan phantom by FBP and DIRECTT, after the phantom was projected over an angular range of 135°, rather than 180°, is shown in Figure 3.5. Both reconstructed images were subsequently projected over the complete 180° angular range. The resulting sinograms are shown next to the respective reconstructed image. The sinograms appear blurrier over the range $[0°, 135°]$, since no projections within this range where used for the reconstruction.

The shapes of the two sinograms in Figure 3.5 differ greatly from one another, mainly because of the effect of the artefacts in the image that was reconstructed by the FBP on the corresponding sinogram. The PCC between the projections of the phantom and each reconstructed image in Figure 3.5 over 180° are plotted in Figure 3.6. Because of the aforementioned artefacts, the PCC of the image that was reconstructed by FBP remains below 1 and fluctuates. The lowest values are located with the angular range for which no projections were included during the reconstruction. In

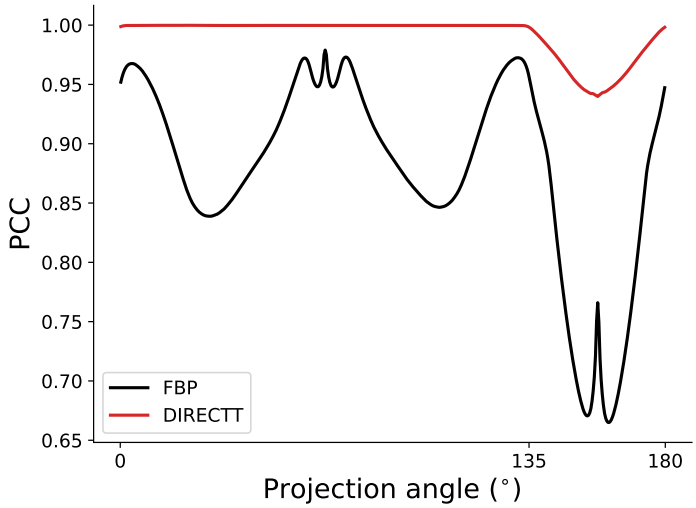

Figure 3.6: The Pearson correlation coefficient (PCC) between the projections of the Shepp-Logan phantom and the Radon transform of the two reconstructed images in Figure 3.5 over 180°.

the case of the image that was reconstructed by DIRECTT, the PCC only decreases below 1 within the range $[0°, 135°]$ but is consistently higher than the PCC of the FBP image.

3.2 No-reference metrics

No-reference metrics evaluate image quality based on statistical features of the assessed image. Examples of such metrics are the *Blind/Referenceless Image Spatial Quality Evaluator* (BRISQUE) [41], the *Natural Image Quality Evaluator* (NIQE) [42], and the *Perception-based Image Quality Evaluator* (PIQE) [57]. These algorithms are trained on datasets of known distortions to assess images. However, their versions that are available with open-source software, such as Matlab [40], are not trained for the images that one typically encounters in CT.

There are, nevertheless, no-reference metrics that are simple to calculate, yet provide useful information on image quality. *Contrast-to-noise ratio* (CNR), for instance, is defined as

$$\mathrm{CNR} = \frac{|S_A - S_B|}{\sigma_0} \tag{3.7}$$

where S_A and S_B are the intensities of two regions of interest, and σ_0 is the standard deviation of the pure image noise. If region B is selected within

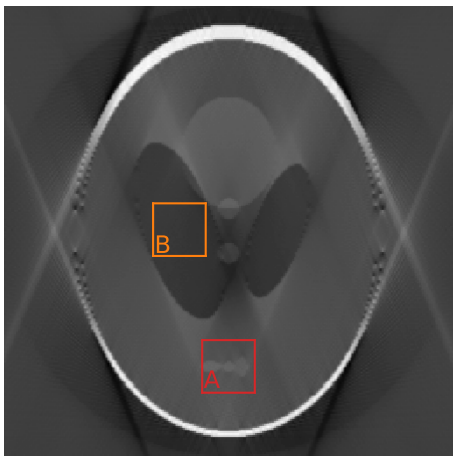

Figure 3.7: Magnification of the image, from Figure 3.7, that was reconstructed by FBP. The contrast-to-noise ratio can be calculated from the regions of interest A and B. Region B corresponds to the background of the image and the standard deviation of its greyscale values are used to estimate the noise.

the image background, the formula takes the form:

$$\mathrm{CNR} = \frac{|S_A - S_B|}{\sigma_B}. \tag{3.8}$$

By definition, an image with little noise will have a high CNR.

The FBP-reconstructed image from Figure 3.7 is shown in greater detail in Figure 3.7. The CNR for Figure 3.7, according to Equation 3.8, is 1.1. The CNR for the same image as reconstructed by DIRECTT (Figure 3.5) is identical.

Another useful metric is the *entropy* of the image. The differential entropy of a probability distribution $f(x)$ is

$$h(f) = -\int f(x) \log f(x) \mathrm{d}x \tag{3.9}$$

If $f(x)$ is approximated with a histogram, the discrete entropy is

$$H(f) = -\sum_{i=1}^{n} f(x_i) \log \left(\frac{f(x_i)}{w(x_i)} \right), \tag{3.10}$$

where $w(x_i)$ is the frequency of the cases in each bin of the histogram [21]. Entropy is influenced by the presence of either noise or blur; homogeneously distributed noise will maximize the outcome of Equation 3.10, while sharp

delta peaks (histogram bars) will minimize it. Therefore, a low entropy is an indication of high image quality [2]. For reference, the entropy of the Shepp-Logan phantom is 0.97. The entropy of the images reconstructed from missing-wedge projections by FBP and DIRECTT is 4.24 and 3.42, respectively.

Chapter 4

Reconstruction from parallel-beam tomography data

4.1 Sample images

Two parallel-beam datasets were acquired at the BAMline [45] of the BESSY synchrotron radiation facility in Berlin, Germany. A pco.4000 CCD camera of 4008×2672 pixels and a nominal pixel size of 9 μm was used for the measurements. The incident cross section was narrowed by a slit system to the detector field-of-view (FoV) in order to reduce detector backlighting [1].

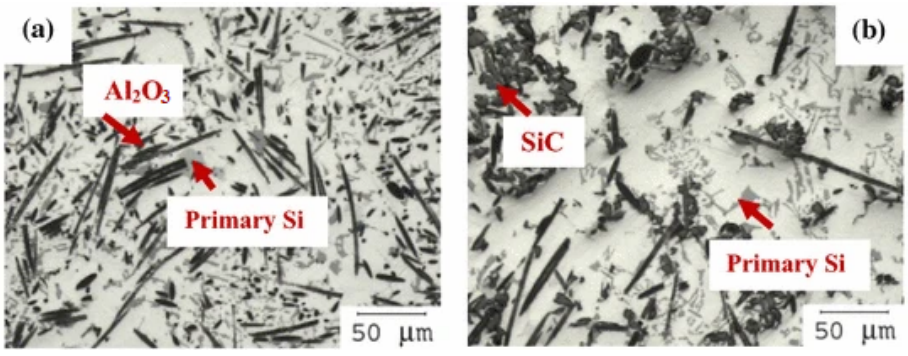

Figure 4.1: Tomograms of two metal matrix composite plates of different compositions. In the sample of (a), the presence of Al_2O_3 fibers is prevalent. In the sample of (b), which will be reconstructed in this chapter, SiC particles are also visible. The figure is reproduced from Reference [9].

Metal matrix composite The first sample was a metal matrix composite (MMC) plate. The MMC was an $AlSi_{12}CuMgNi$ alloy reinforced with 7 vol. % of Al_2O_3 short fibres and 15 vol. % SiC particles (Figure 4.1). A cylinder with a diameter of 1 mm was extracted by a billet, which had been produced by squeeze casting. Monochromatic radiation of 25 keV was selected for the measurement and 3000 projections were acquired over 180°. The acquisition time per projection was 3 s. A 20× magnification of the camera system resulted in a linear voxel size of 0.44 μm [9].

Invar grid The second sample was a grid made of Invar, a nickel-iron alloy that is also known generically as **FeNi36**. The sample has a large aspect ratio: its surface is 1.1 mm × 2.8 mm, while its thickness is 20 μm. Forty columns and 20 rows of circular apertures formed the grid structure. The apertures had a diameter of 0.18 mm. Monochromatic radiation of 30 keV was selected for the measurement and 3000 projections were acquired over 180°. The acquisition time per projection was 2 s. A 4× magnification resulted in a linear voxel size of 2.2 μm.

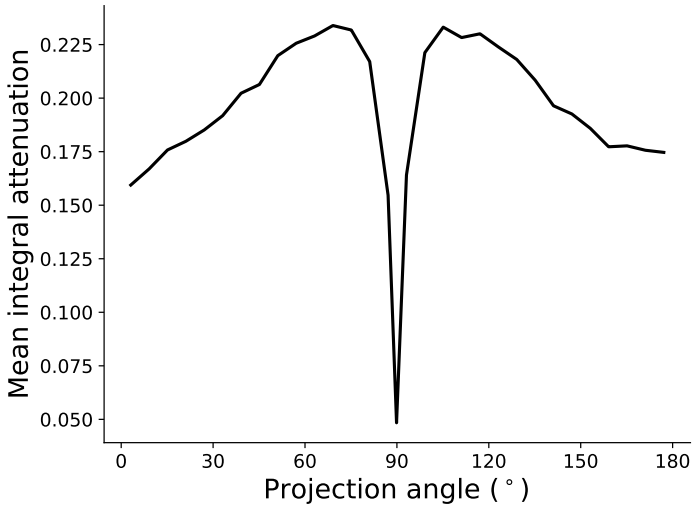

Figure 4.2: Mean attenuation of the X-ray beam as a function of the projection angle θ during the measurement of the invar grid. The sharp drop in the range $[86°, 94°]$ is attributed to the unsuitable dynamic range of the detector that was set for the initial orientation of the sample.

The dynamic range of the detector was set when the longer side of the grid was parallel to the detector. However, after the grid had rotated 90° relative to its initial orientation, approximately 93% of the photons reached the detector without interacting with the grid. For the projections that

correspond roughly to the angular range $[86°, 94°]$, the dynamic range of the detector did not allow the accurate recording of the attenuation signal (Figure 4.2).

4.2 Results and discussion

4.2.1 Simulation of a missing-wedge measurement

A single horizontal slice of the MMC sample was reconstructed by DIRECTT from the projections that correspond to a single row v of the 4008×2672 detector. The projections, in the form of a sinogram, and the corresponding histogram are shown in Figures 4.3a and 4.4, respectively. There are two distinguishable parts in the histogram: a narrow peak, which corresponds to the part of the beam that reaches the detector without being attenuated, and a wider range of values that correspond to the MMC.

DIRECTT was programmed to run until the condition

$$\frac{||P - AX^k||}{||P||} \leq 0.05. \tag{4.1}$$

was satisfied. This required 40 iterations. A uniform disk C with a diameter of 1.2 mm was modelled in order to calculate the value of β_k (Equations 2.2, 2.3). The value of α (Equation 2.2) was set to 12. The residual sinogram at the termination of DIRECTT is shown in Figure 4.3b. All the values are around zero. The comparison of the corresponding histogram in Figure 4.4 with that of the measured projections confirms that the residual projections consist mainly of noise.

The same slice of the MMC sample was also reconstructed by FBP, as well as 120 iterations of SIRT, and 40 iterations of CGLS. The iterative algorithms were also terminated after the condition of Equation 4.1 had been met. The images that were reconstructed by each of the four algorithms are shown in Figure 4.5. A common 600×600 μm^2 region of interest (ROI) around the centre of each image in Figure 4.5 is shown in 4.6.

The image that was reconstructed by FBP appears to be noisy. The iterative algorithms have suppressed the noise in the reconstructed images. The values of two no-reference quality metrics, the CNR and the entropy H, are listed in Table 4.1 for all four images. The values for the image that was reconstructed by DIRECTT are better by a significant margin, which is largely attributed to the fact that the background of the image is virtually noise-free.

The same projections of Figure 4.3a were used to simulate a missing-wedge measurement. Specifically, the reconstruction of the slice was attempted using only 2000 of the 3000 acquired projections, which corresponded to the angular range $[0°, 120°]$. The images that were reconstructed

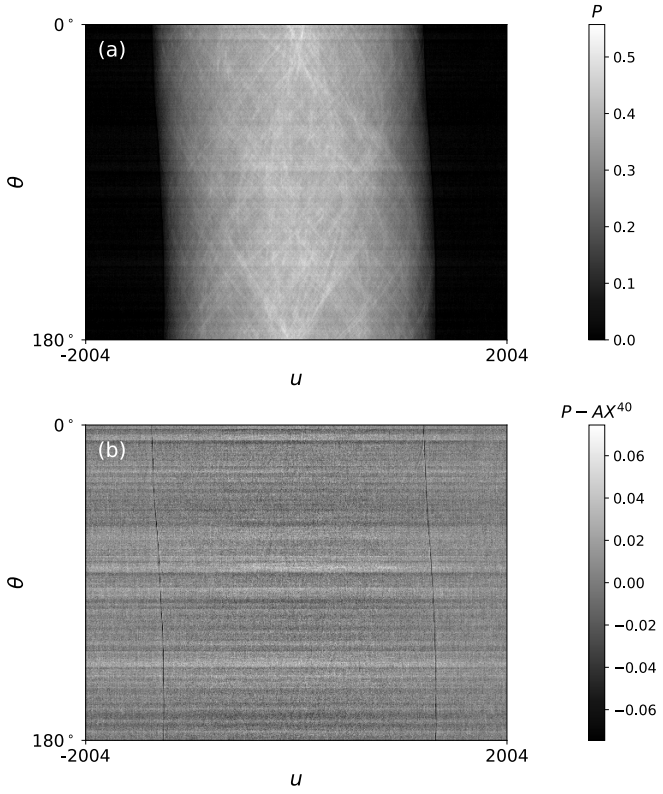

Figure 4.3: (a) Projections corresponding to a single horizontal slice of the metal matrix composite sample. (b) Residual projections of the same slice after 40 iterations of DIRECTT.

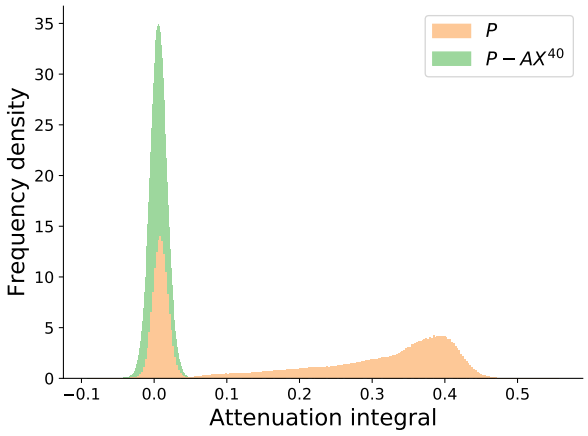

Figure 4.4: Histograms of the values in the sinograms of Figures 4.3a and 4.3b.

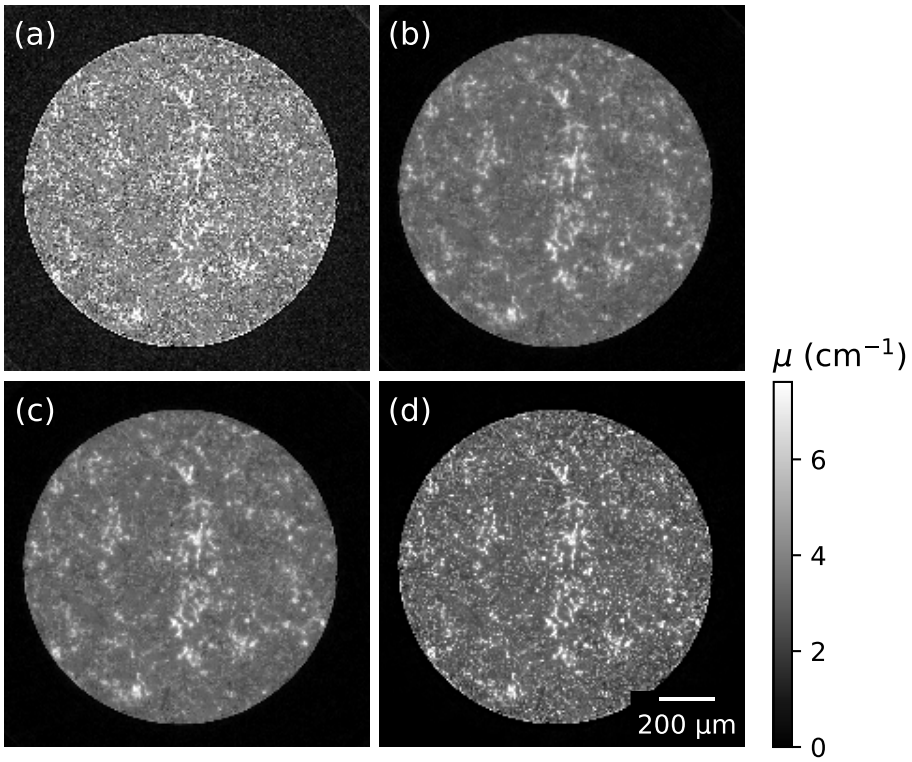

Figure 4.5: Reconstruction of a horizontal slice of the metal matrix composite sample from 3000 projections by (a) FBP, (b) 60 iterations of SIRT, (c) 25 iterations of CGLS, and (d) 40 iterations of DIRECTT. For reference, the theoretical μ for the nominal density of Al_2O_3 and SiC (2.7 g·cm^{-3} and 3.2 g·cm^{-3}, respectively) are 5 cm^{-1} and 5.7 cm^{-1}.

Table 4.1: The contrast-to-noise ratio (CNR) and the entropy of each image in Figure 4.5.

Algorithm	CNR	Entropy H
FBP	7.9	4.9
SIRT	20.6	3.9
CGLS	27.1	3.8
DIRECTT	93.8	2.7

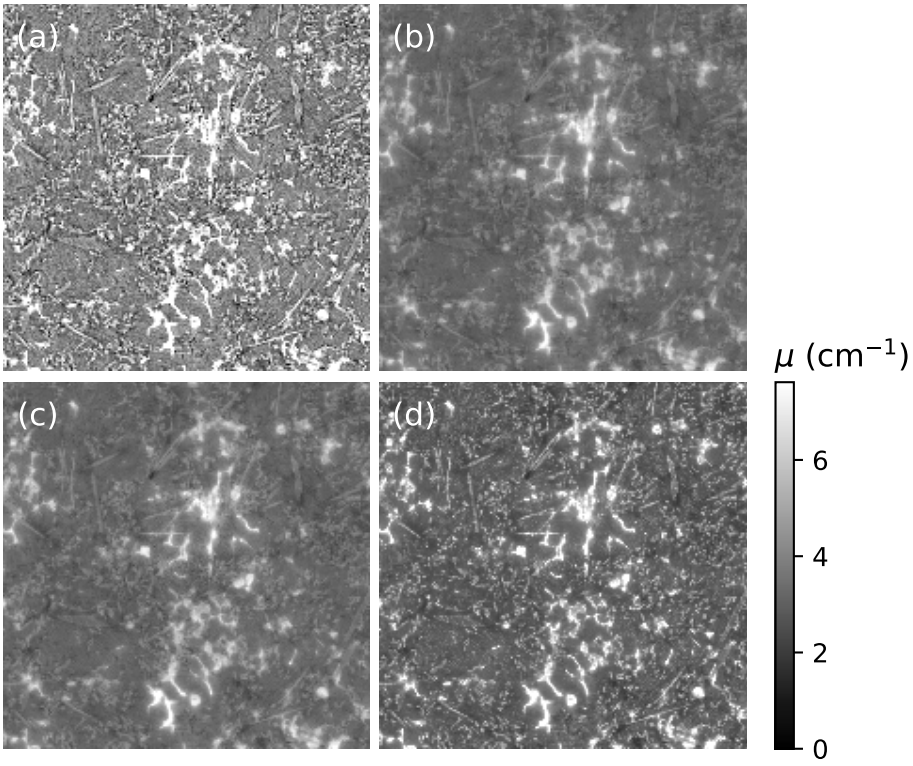

Figure 4.6: A 600×600 μm^2 region of interest around the centre of each image in Figure 4.5.

by FBP, SIRT, CGLS, and DIRECTT are all shown in Figure 4.7. A common 600×600 μm^2 ROI around the centre of each image in Figure 4.7 is shown in 4.8. The three iterative algorithms were terminated after the condition of Equation 4.1 had been met. Each performed more iterations than they had in the case of the full dataset. SIRT performed 140 iterations, CGLS performed 70, and DIRECTT performed 60.

The CNR and the entropy H of each image in Figure 4.7 are listed in Table 4.2. The values of both metrics are again better for the image that was reconstructed by DIRECTT. The quality of the reconstructed images was also assessed using two full-reference metrics, the MSE and the SSIM. It has been argued in Chapter 3 that, when the ground truth is not available, earlier reconstructed data of proven quality may serve as the reference instead. Among the images shown in Figure 4.5, which were reconstructed from the full dataset, the image reconstructed by CGLS was chosen as the reference based on its higher CNR and lower entropy (Table 4.1). Although the values of both metrics are better for the image reconstructed by DIRECTT, the

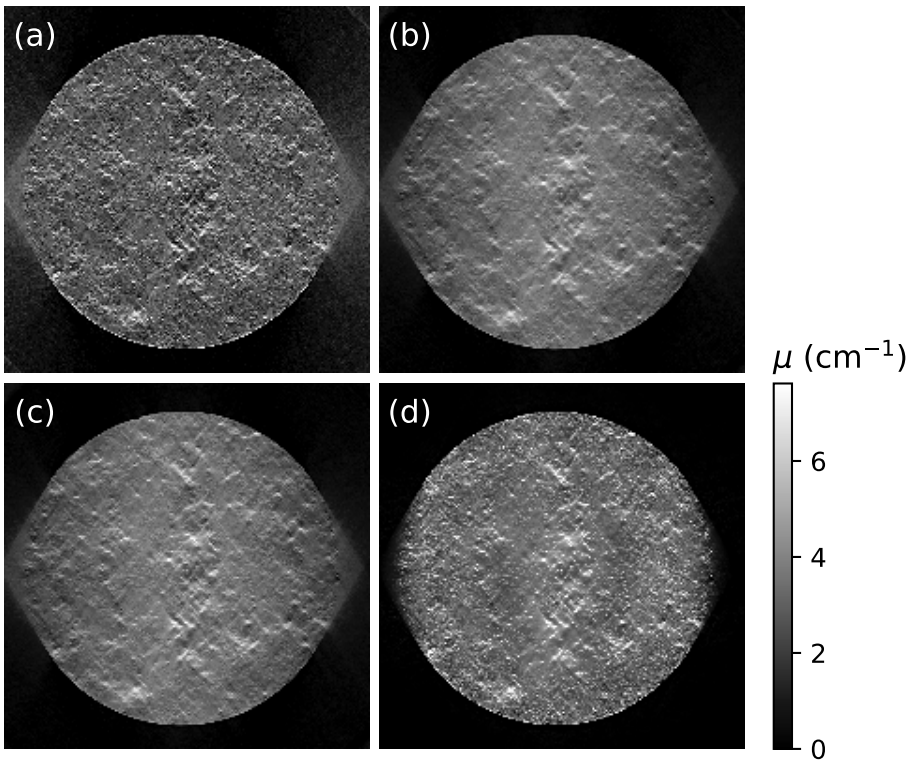

Figure 4.7: Reconstruction of a horizontal slice of the metal matrix composite sample from projections that corresponded to the angular range $[0°, 120°]$. The images were reconstructed by: (a) FBP, (b) 175 iterations of SIRT, (c) 80 iterations of CGLS, and (d) 60 iterations of DIRECTT.

Table 4.2: The contrast-to-noise ratio (CNR) and entropy of each image in Figure 4.7, and their mean squared error and structural similarity index metric in reference to the image in Figure 4.5 that was reconstructed by CGLS.

Algorithm	CNR	Entropy H	MSE (cm^{-2})	SSIM
FBP	2.5	5.0	1.06	0.39
SIRT	7.2	4.6	0.22	0.75
CGLS	7.9	4.6	0.22	0.75
DIRECTT	32.5	2.8	0.22	0.78

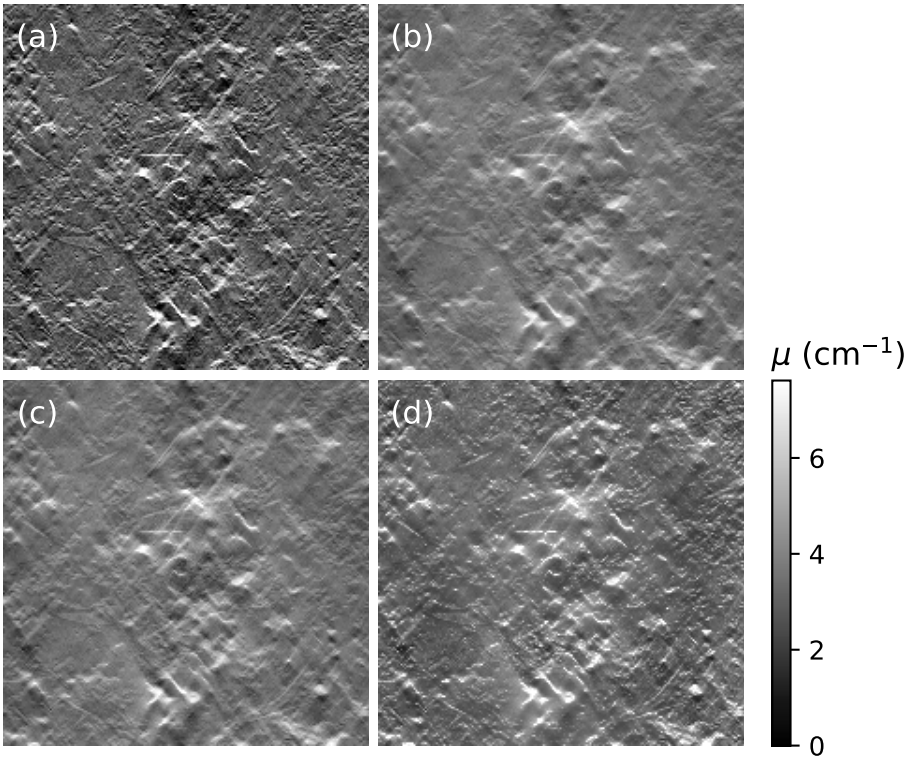

Figure 4.8: A 600×600 μm^2 region of interest around the centre of each image in Figure 4.7.

image was chosen as the reference in order to remove any bias in favour of the DIRECTT.

The values of MSE and SSIM for each image of Figure 4.7 are listed in Table 4.2. The higher SSIM value for the image that was reconstructed by DIRECTT is attributed to the fact that the algorithm has performed better in preserving the shape of the sample despite the missing wedge. This is strictly a result of the implementation of DIRECTT. No additional geometric constraints, such as masks, were imposed on the image.

The perception that the image that was reconstructed by DIRECTT is the most accurate is reinforced when the PCC between the full dataset of projections and the Radon transform, over the full 180°, of all reconstructed images of Figure 4.7 is calculated. It is evident from Figure 4.9 that, in the case of the images that were reconstructed by FBP, the PCC decreases sharply in the range $[120°, 180°]$. The images by CGLS and SIRT have a higher correlation which, however, still decreases noticeably in the range of the missing projections. On the other hand, the PCC that corresponds to

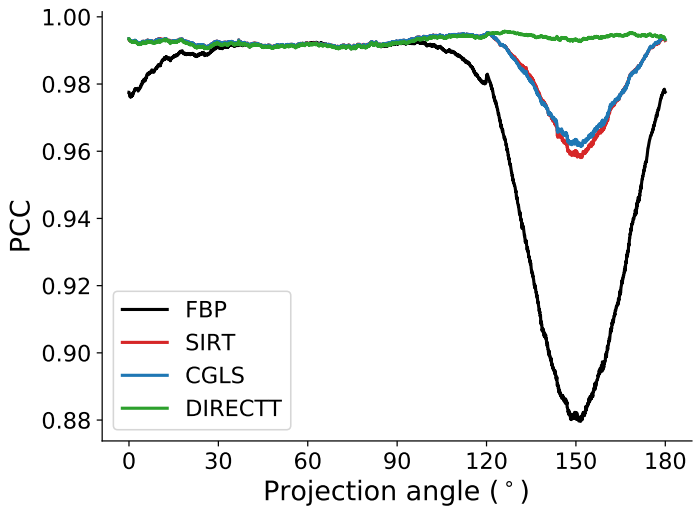

Figure 4.9: Pearson correlation coefficient (PCC) as a function of the projection angle. The coefficient is calculated for the full dataset of projections of the metal matrix composite slice and the forward projection of the images that were reconstructed from the projections that corresponded to the angular range $[0°, 120°]$ by different algorithms.

DIRECTT remains near 1 over the full range of 180°.

4.2.2 Reconstruction of a sample with large aspect ratio

In section 4.1, it was explained that, because of the dynamic range that was selected for the detector during the measurement of the Invar grid, it was not possible to record an accurate attenuation signal within the angular range $[86°, 94°]$ (Figure 4.2). Instead of allowing them to affect the reconstruction in a negative way, the corresponding projections (100 out of the 3000 that were acquired) were discarded. The reconstruction of the grid from the remaining 2900 projections presents challenges that are similar to those of a missing-wedge measurement.

The grid was reconstructed by FBP, SIRT, CGLS, and DIRECTT. The three iterative algorithms performed 300, 250, and 300 iterations, respectively. Regarding the implementation of DIRECTT, a cuboid C with dimensions 3.15 mm × 8.4 mm × 0.06 mm was modelled in order to calculate the value of β_k; α was set to 1.

Two cross sections of the volume that was reconstructed by DIRECTT are shown in Figure 4.10. The corresponding cross sections of the volumes that were reconstructed by the other three algorithms are not shown since, at this scale, the differences among the images would not be easily distin-

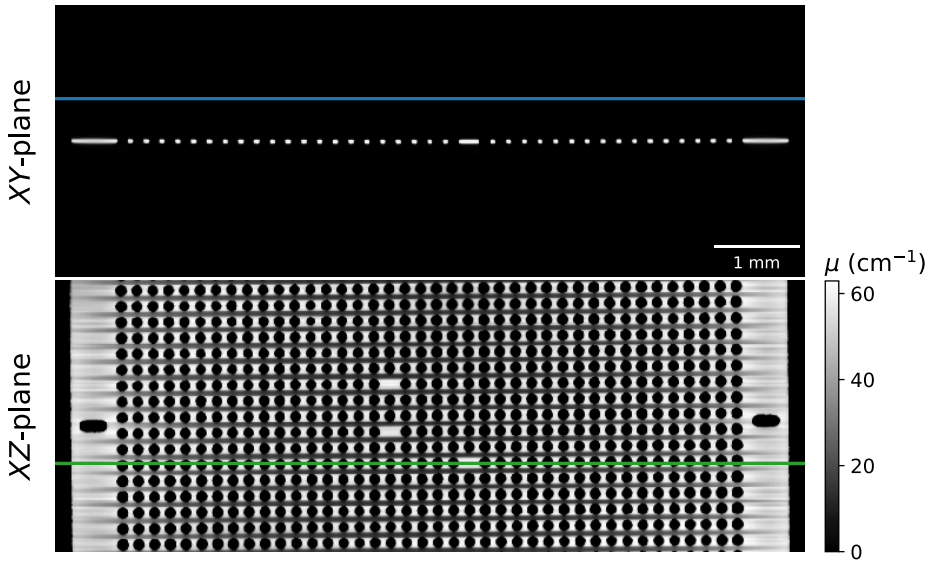

Figure 4.10: Orthogonal views of the volume of the invar grid that was reconstructed by DIRECTT. The green line along the XZ-view refers to the relative position of the XY-view. The blue line along the XY-view refers to the relative position of the XZ-views of Figure 4.11. For reference, the theoretical μ of Invar for its nominal density of 8 g·cm^{-3} is 71 cm^{-1}.

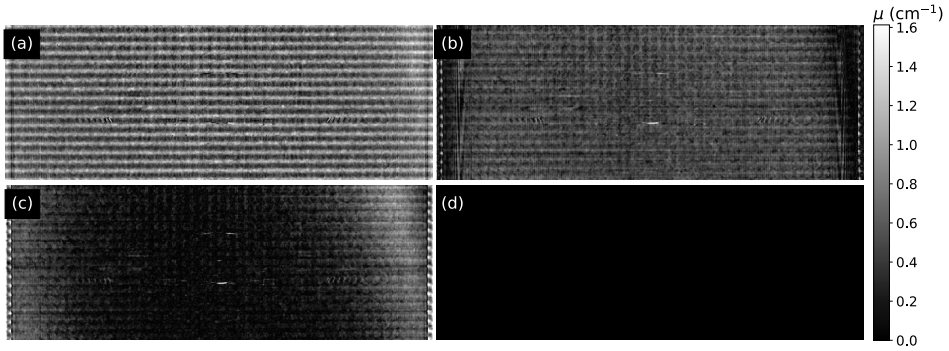

Figure 4.11: Images from the volumes of the grid that were reconstructed by (a) FBP, (b) SIRT, (c) CGLS and (d) DIRECTT. The images correspond to the blue line in Figure 4.10. At $\Delta y = 0.4$ mm from the grid, only the volume that was reconstructed by DIRECTT is entirely devoid of 'ghost images'.

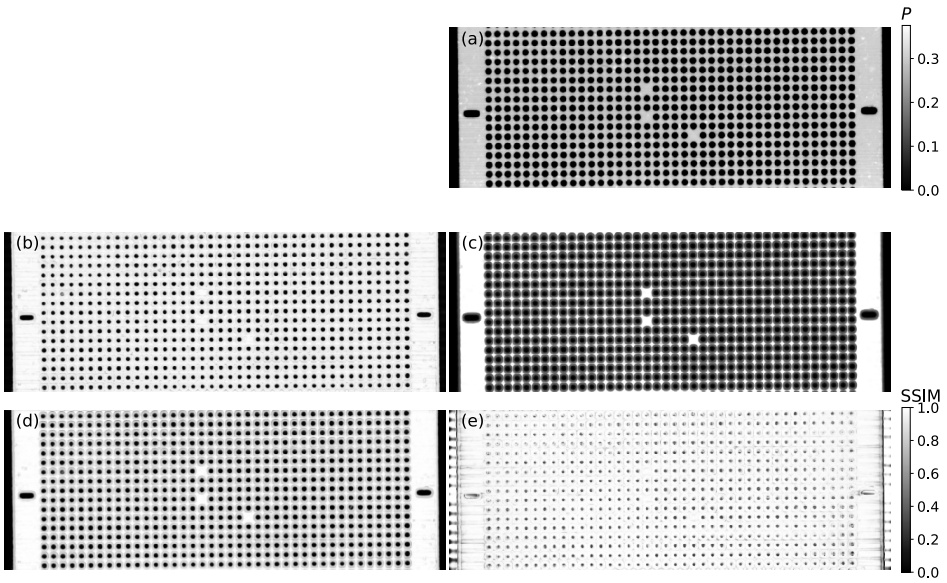

Figure 4.12: (a) The measured projection of the grid at angle $\theta = 0$. (b-e) The *structural similarity index metric* image between the measured projection and the corresponding Radon transform of the volume that was reconstructed by (b) FBP, (c) SIRT, (d) CGLS, and (e) DIRECTT.

guishable. Information about the qualitative differences among the volumes can be extracted by calculating their CNR and entropy, the values of which are listed in Table 4.3. The volume that was reconstructed by DIRECTT has both the highest CNR and the lowest entropy.

Images from each of the four reconstructed volumes are shown in Figure 4.11. The images correspond to the blue line in Figure 4.10. At $\Delta y = 0.4\,\text{mm}$ from the grid, only the volume that was reconstructed by DIRECTT is entirely devoid of artefacts. While, at that distance from the grid, the volumes should be empty ($\mu = 0$), the cross sections through the volumes other than DIRECTT reveal 'ghost images'. This is a further indication that DIRECTT has performed better in preserving the shape of the grid. Note that the zero image is not the result of the application of a mask to the volume after the algorithm was terminated. It is rather a result of the implementation of DIRECTT.

It was explained in Chapter 3 that, when real samples are reconstructed, there is no available reference to compare the reconstructed images to and that the acquired projections can be used for the same purpose instead. Moreover, the correlation coefficient was suggested as a local metric that can be used to compare the Radon transform to the acquired projections.

Because of the shape of the grid, which results to several projections

Table 4.3: The contrast-to-noise ratio and entropy of each reconstructed volume, and the *structural similarity index metric* (SSIM) between the Radon transform of each volume and the measured projections.

Algorithm	CNR	Entropy H	SSIM(P, AX)
FBP	1.1	2.8	0.79
SIRT	1.7	3.5	0.46
CGLS	2.6	3.6	0.71
DIRECTT	5.3	1.4	0.92

consisting mainly of background values, the calculation of the correlation coefficient, similar to Figure 3.4, would not return meaningful results. Instead, the assessment may be focused on projections that corresponds to views near $\theta = 0$ or $\theta = \pi$, when the grid is projected on most of the detector. In this case, the assessment can be carried out by calculating the *SSIM image* that compares the acquired projection and the Radon transform for the specific angle.

The SSIM images for each reconstructed volume after it has been projected at $\theta = 0$ are shown in Figure 4.12. The respective values of the metric are listed in Table 4.3. In the case of the volume that was reconstructed by DIRECTT, most pixels in the corresponding SSIM image have values near 1. The SSIM images that correspond to the other volumes have a higher number of pixels with values near 0, particularly where the apertures are projected and also in the background of the projections. This is an indication of a less precise reconstruction of the apertures, as well as noise in the corresponding reconstructed volumes.

Chapter 5

Reconstruction from cone-beam tomography data

5.1 Sample images

A concrete rod was scanned with a GE v|tome|x L300 scanner operated by Division 8.5 of BAM. The shape of the rod was a cylinder with a radius of 30 mm. An example of a similar, but thicker, sample is shown in Figure 5.1. A PerkinElmer detector of 2024×2024 pixels and a pixel size of 0.2 mm was used for the measurement. The source-detector distance was SD = 1018 mm. A 0.5 mm Cu prefilter was placed in front of the source.

Two different datasets of 3000 projections over 360° were acquired for the same sample:

1. During the first measurement, the source-to-object distance was SO = 81.4 mm. A not-to-scale geometric representation of the measurement is shown in Figure 5.2a. The width of the rod lay fully within the FoV for all projections. Conversely, the inverse conical area, which is defined by the solid and dashed red lines in Figure 5.2, in the lower part of the sample did not lay within the FoV for all projections. This area, as will be shown also in the next section, cannot by definition be fully reconstructed by FDK [18]. The rod extended all the way to the lower edge of the FoV but, at the same time, not to its upper edge.
   The voltage and current settings of the source were set to 140 kV and 80 μA, respectively. The acquisition time per projection was 6 s. The relation between the source-object and source-detector distances resulted in a 12.5× magnification and a voxel size of 16 μm [38].

2. The second measurement was a ROI measurement. The source-to-object distance was SO = 40.7 mm. A not-to-scale geometric representation of the measurement is shown in Figure 5.2b. Because of the proximity of the rod to the source, its width never lay fully within the

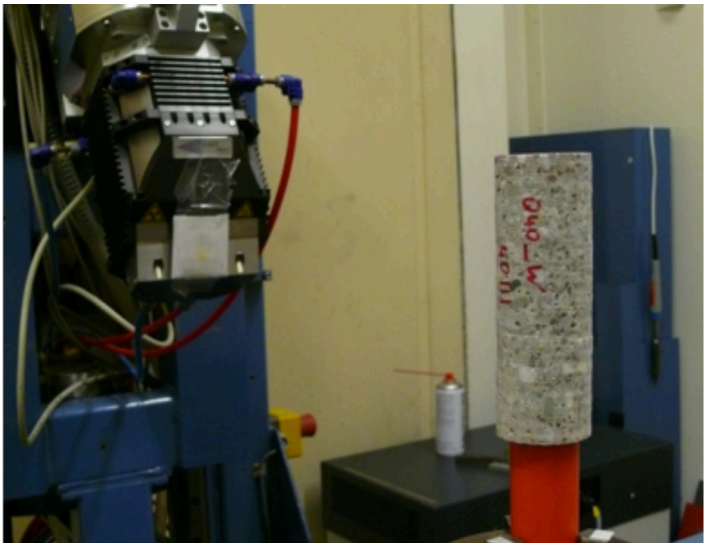

Figure 5.1: Photograph of a computed tomography scanner, which was designed and is operated by BAM, with a concrete rod placed on the rotating table. The rod that is pictured is thicker than the rod that will be reconstructed in this chapter. The figure was reproduced from Reference [25].

FoV. In this case the rod extended all the way to both the upper and lower edges of the FoV. Therefore, there is an inverse conical area that cannot be fully reconstructed by FDK in both directions.
The voltage and current settings of the source were set to 140 kV and 70 μA, respectively. The acquisition time per projection was 6 s. The relation between the source-object and source-detector distances resulted in a 25$\times$ magnification and a voxel size of 8 μm.

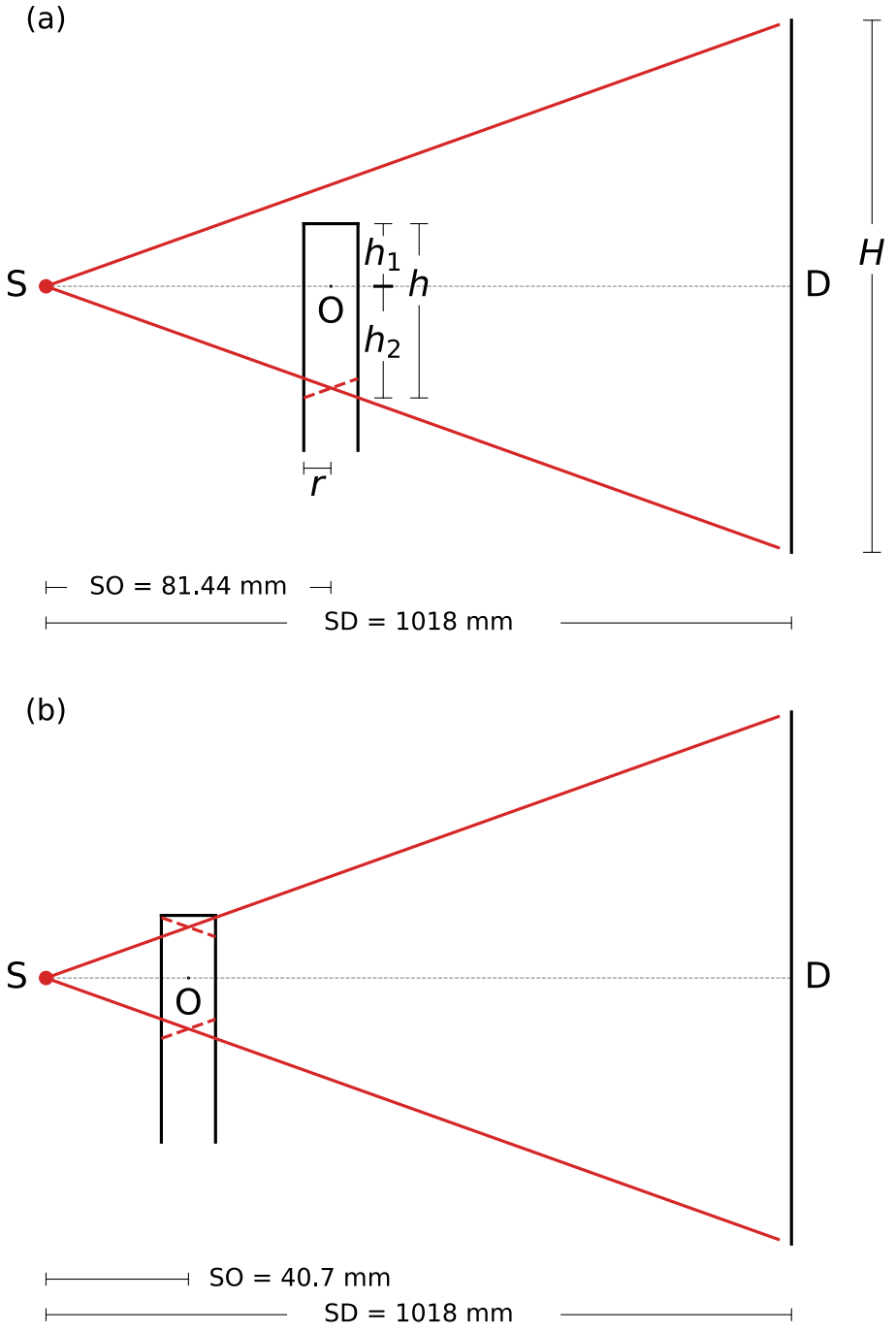

Figure 5.2: Geometric representation of the (a) full-width and (b) region-of-interest measurements of the concrete rod. The setup is not pictured to scale.

5.2 Results and discussion

5.2.1 Full-width measurement

It has been explained in Chapter 2 that the model object C serves a dual role for the reconstruction from cone-beam data with DIRECTT: Its forward projection is computed once and used, during each iteration, to correct the volume following the back-projection (Equation 2.4) and to determine the voxels the value of which will be updated (Equations 2.2 and 2.3).

In the case of the concrete rod, it is easy to define a uniform object C the shape of which matches the shape of the sample. The rod is cylindrical, which is the most common sample shape in CT measurements for non-destructive testing and materials science [4, 8, 10, 13]. Even if its dimensions are not already known from the acquisition stage, as would typically be the case, they can be determined from the measured data. First, its radius can be determined from its projections, one of which is shown in Figure 5.3a. Specifically, it can be determined as half the distance between the two peaks in the plot of $\left|\mathrm{d}\overline{P}(u)/\mathrm{d}u\right|$ (the absolute value of the derivative of the mean integral attenuation along the detector columns u) in Figure 5.3b. Considering that the size of the detector pixels was 0.2 mm and that the measurement resulted in a magnification of 12.5×, the radius r of the rod, and the object C, is estimated to be equal to 14.74 mm.

The height h of the part of the rod that lay within the FoV at any moment, during the acquisition, is equal to the sum of h_1 and h_2. These are the heights of the parts of the rod that lay above and below the source plane, respectively. Using basic geometry concepts, it can be shown [39] that

$$h_2 = \frac{\mathrm{SO} + r}{\mathrm{SD}} \cdot \frac{H}{2}, \tag{5.1}$$

where $H = 404.8\,\mathrm{mm}$ is the height of the detector. Hence, $h_2 = 19.12\,\mathrm{mm}$.

The height h_1 can be estimated from the result of the back-projection of the measured data, rather than the data itself, as was the case for the radius r. Specifically, it can be derived by the inflection point of $\mu(z)$. A vertical cross section through the centre of the volume which the back-projection results in is shown in Figure 5.3c. From the high peak in the plot of $|\mathrm{d}\overline{\mu}(z)/\mathrm{d}z|$ (the absolute value of the derivative of the mean attenuation coefficient along the axis z) in Figure 5.3d, it is estimated that $h_1 = 12.66\,\mathrm{mm}$. Therefore, the total height is $h = 31.78\,\mathrm{mm}$.

After the uniform object C has been defined, its forward projection is computed and the result is back-projected. The volume that the back-projection results in, after it has been normalized for the slice that is parallel to the source plane, is the model M (Equation 2.4) of artefacts that are associated with the projection geometry and the geometry of the sample. Orthogonal cross sections through the concrete rod after the back-projections

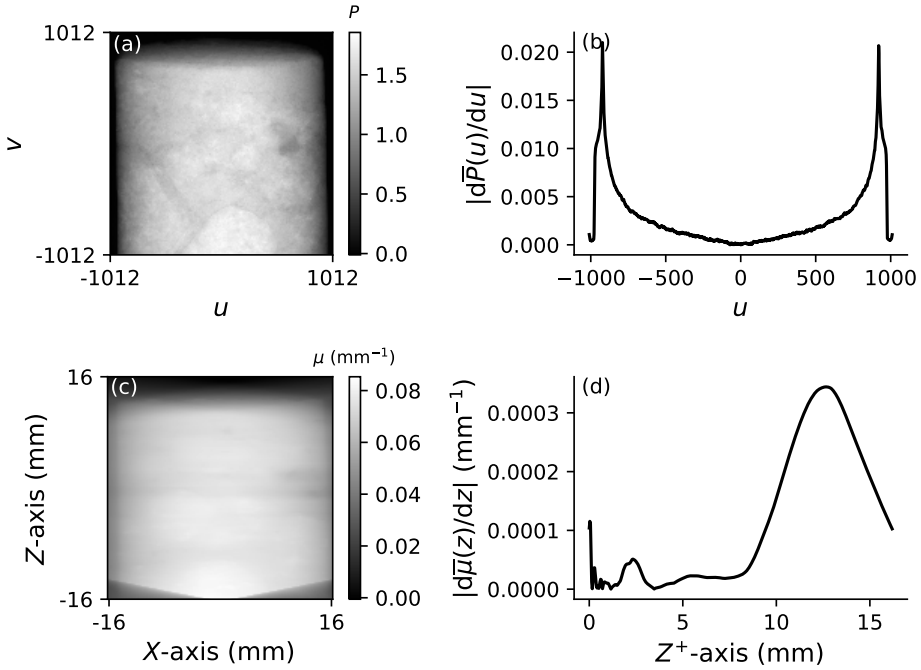

Figure 5.3: (a) A projection of the concrete rod. (b) Absolute value of the derivative of the mean integral attenuation along the detector columns u. The diameter of the rod can be derived from the distance between the two peaks. (c) Vertical cross section through the centre of the volume that the back-projection of the data results in. (d) Absolute value of the derivative of the attenuation coefficient along the positive part of axis z. The position of the high peak is used to derive the height of the part of the rod that extends above the source plane (h in Figure 5.2).

of the measured data and through the corresponding model M are shown in Figure 5.4. The qualitative relation between the two sets of images is obvious. Performing the Hadamard division of the two, the artefacts in the volume are suppressed and the voxels the value of which will be updated in the volume estimate are determined. These steps are repeated during each iteration of DIRECTT without the need to compute an updated M.

Cross sections through the volumes that were reconstructed by FDK, 200 iterations of SIRT, 60 iterations of CGLS, and 200 iterations of DIRECTT are shown in Figure 5.5. For the implementation of DIRECTT, the value of α was set to 6.4. The relative position of the cross sections in Figure 5.5 corresponds precisely to the views in Figure 5.4. The CNR and entropy of each volume are listed in Table 5.1. The artefacts that are associated with

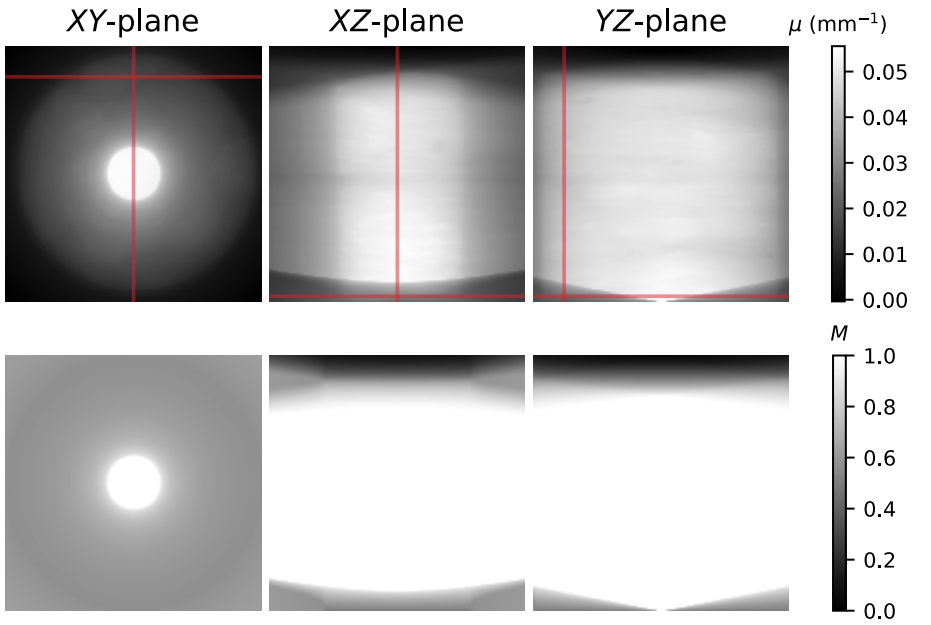

Figure 5.4: Orthogonal cross sections through the concrete rod after the back-projections of the measured data (top row) and through the corresponding model M (bottom row). The red lines indicate the position of each cross section in relation to the other two.

cone-beam CT are prevalent in the volume that was reconstructed by FDK, which is also noisy. These shortcomings of FDK are reflected on the low CNR and the high entropy of the volume.

The iterative algorithms appear to have suppressed these artefacts, albeit in varying degrees. The greyscale values in the volume that was reconstructed by SIRT are consistent along the z-axis but the images are not very sharp. The volume that was reconstructed by CGLS is sharper. However, it suffers from severe ring-like artefacts, which are located at the border between the part of the sample that always lies within the FoV and its part that only lies within it partially (i.e., not for all projection angles). With the exceptions of these artefacts, the greyscale values are consistent along the z-axis. The volume that was computed by DIRECTT is sharp and largely noise-free, as attested by its high CNR and low entropy. Its greyscale values are also consistent along the z-axis.

Profiles across the centre of each XY-slice of Figure 5.5 are plotted in Figure 5.6. The profiles, in their respective volumes, correspond to the voxels marked with the green line in the XY-slice of the DIRECTT-reconstructed volume in Figure 5.5. An accurate profile should have a square shape with

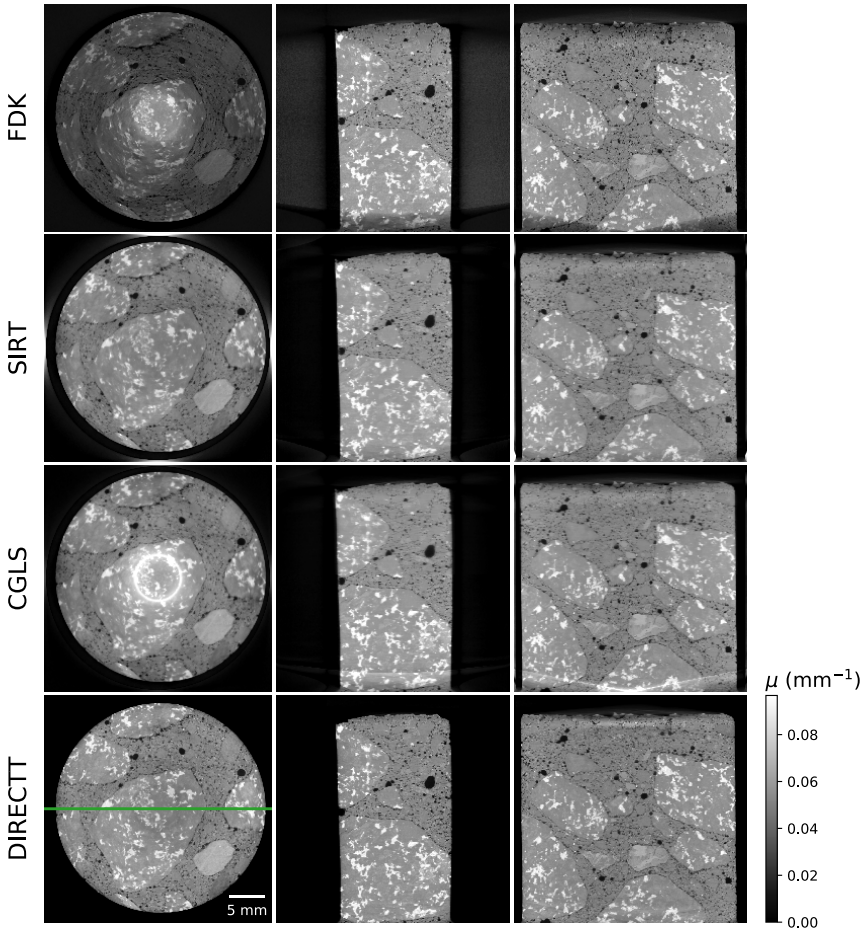

Figure 5.5: Orthogonal cross sections through the volume of the concrete rod that was reconstructed by FDK, 200 iterations of SIRT, 60 iterations of CGLS, and 200 iterations of DIRECTT. The cross sections correspond precisely to those from Figure 5.4. The green line in the XY-slice of the DIRECTT-reconstructed volume in Figure corresponds to the profiles that are plotted in Figure 5.6.

Table 5.1: The contrast-to-noise ratio and the entropy of each volume in Figure 5.5.

Algorithm	CNR	Entropy H
FDK	4.8	5.1
SIRT	7.2	4.8
CGLS	9.4	4.8
DIRECTT	23.8	3.4

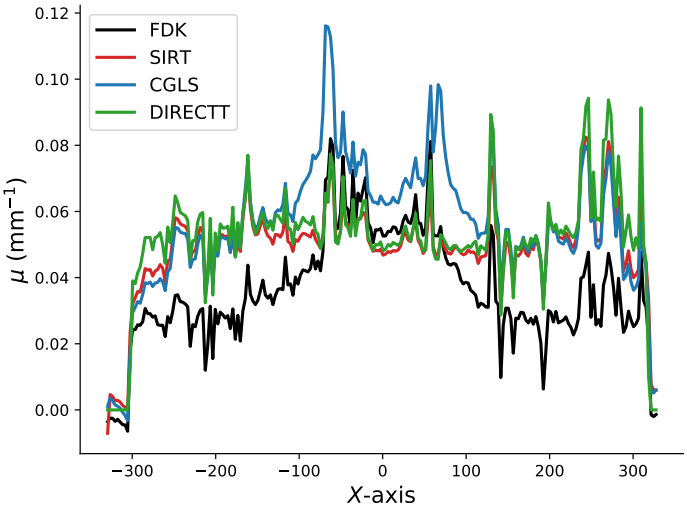

Figure 5.6: Profiles across the centre of each XY-slice of Figure 5.5. The profiles, in their respective volumes, correspond to the voxels marked with the green line in the XY-slice of the DIRECTT-reconstructed volume in Figure 5.5.

modulation that corresponds to the composition of the sample. Because of the cone-beam artefacts, the values of μ near the edges are lower and the profile that corresponds to FDK deviates from the described shape. The iterative algorithms have largely suppressed these artefacts. However, in the case of the volumes that were reconstructed by SIRT and CGLS, the outer edges are still more blurred than the centre of the slice. The presence of artefacts at the edges of the inverse conical area near the bottom of the volume that was reconstructed by CGLS has a visible contribution to the respective profile, which is plotted in Figure 5.6 in blue.

Simulation of sparse-sampling measurements

The same dataset was used to simulate sparse-sampling measurements. By progressively and evenly removing projections, the reconstruction of the concrete rod was attempted from five under-sampled datasets of 1500, 1000, 750, 600, and 500 projections. Each dataset still represented a full rotation of the sample (no missing wedge) but with only a fraction of the original projections.

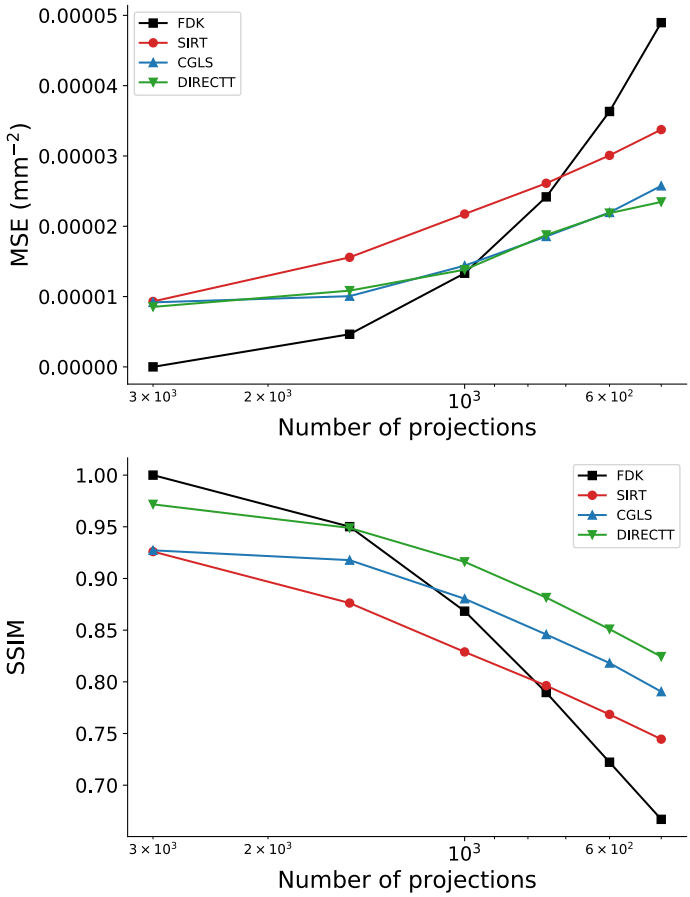

Figure 5.7: *Mean squared error* (MSE) and *structural similarity index metric* (SSIM) of each reconstructed volume of the concrete rod. Six datasets that contained between 500 and 3000 projections were reconstructed, each by FDK, SIRT, CGLS, and DIRECTT. The volume that was reconstructed by FDK from the full dataset was used as the reference for the calculation of both metrics.

The rod was reconstructed from each dataset by all four previously used

algorithms. The number of iterations that the iterative algorithms needed to perform generally decreased along with the decrease in the number of projections. SIRT performed between 70 and 160 iterations until it met the termination condition, CGLS between 50 and 60, and DIRECTT between 140 and 175.

The quality of each reconstructed volume was assessed by calculating their MSE and SSIM. Since the ground truth for the sample is not known, one of the volumes from Figure 5.5 had to serve as the reference for the calculation of the two metrics. Among the four, the volume that was reconstructed by FDK was of lesser quality than either of the other three, with respect to the metrics of Table 5.1. Nevertheless, FDK is accepted as the standard algorithm for reconstruction from cone-beam data. Therefore, using the volume that was reconstructed by FDK as the reference is reasonable.

More specifically, the MSE and SSIM were calculated for regions of dimensions $(16.2\text{ mm})^3$ around the centre of each volume. All voxels within these regions corresponded to the material (including pores) but not the background. Had the metrics been calculated for the whole reconstructed volume, the calculation would have also included noise from the background of the sample. In that case, the calculations would have skewed the results in favour of FDK or any algorithm that fails to suppress the noise during the reconstruction.

The MSE and SSIM of each reconstructed volume are plotted in Figure 5.7. Obviously, the volume that was used as reference has the best possible values fro both metrics (0 for MSE, 1 for SSIM) when compared to itself. Nevertheless, both metrics agree that the quality of the reconstruction by FDK, among all four algorithms, decreases the fastest as a function of the decreasing number of available projections. According to the MSE, CGLS and DIRECTT perform the best. According to the SSIM, there is a clear advantage in using DIRECTT.

Correction of severe ring artefacts

Another challenge that is addressed is the suppression of severe ring artefacts. Such artefacts may be caused by defective detector pixels or, in the case of synchrotron tomography, defects or impurities of the scintillator crystals [6]. Several methods have been proposed for the corrections of ring artefacts, ranging from the standard flat-field correction [50] to processing of the projections during the reconstruction [6] and post-processing of the reconstructed images [52]. Regarding the implementation of DIRECTT, the ring artefacts can be modelled in the model M and therefore corrected during the reconstruction.

A rather extreme case of a ring artefact was simulated for the slice of the concrete rod that was parallel to the source plane. In the simulated case, 40

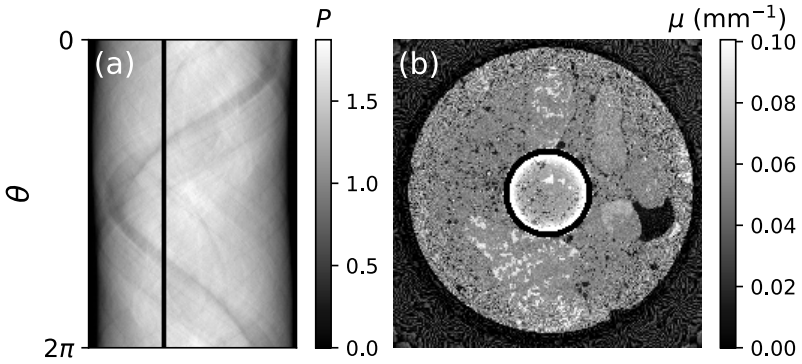

Figure 5.8: (a) Projections of the slice of the detector row that, during the measurement, was parallel to the source plane. The case that 40 consecutive pixels of the corresponding detector row were defective is simulated. (b) Reconstruction of the slice from the sinogram in (a) by FDK.

consecutive pixels of a detector row would be defective. The values of the defective pixels would be discarded and replaced with zero, resulting in the sinogram of Figure 5.8a.

The slice that is reconstructed by FDK from the sinogram is shown in Figure 5.8b. In addition to the significant loss of information because of the ring artefact, the image has an overall high level of noise. While the CNR of the volume in Figure 5.5 that was reconstructed by FDK was 4.8 (Table 5.1), the CNR of the slice in Figure 5.8b is only 1.9. The MSE of the slice in reference to the corresponding slice of the volume that was reconstructed by FDK in Figure 5.5 is 3.8×10^{-4} mm^{-2}. Its SSIM is 0.83.

For the current version of DIRECTT, only a simple back-projection is performed. The result of this operation for the sinogram of Figure 5.8a is shown in Figure 5.9a. For the implementation of the algorithm, it is also required that the Radon transform of a uniform object C is computed. In this case, C is a disk of radius 14.74 mm. However, in this case, the exact same pixels that were discarded in Figure 5.8a are also discarded in the projections of C. The model M for the reconstructed slice that is computed from these projections is shown in 5.9b. The qualitative relation between the result of the back-projection and the model is obvious.

During the first iteration of DIRECTT, the Hadamard division of the slice in Figure 5.9a by the model M is performed. Following this operation, the pixels of the reconstruction slice the values of which will be updated are identified. In subsequent iterations, the result of the back-projection of the residual sinogram is also divided by M.

The final result of DIRECTT is shown in Figure 5.10a. No ring artefact

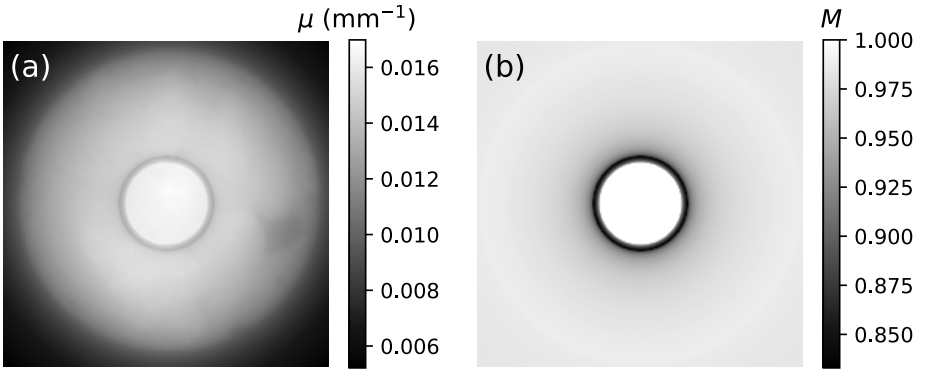

Figure 5.9: (a) Result of the back-projection of the sinogram in Figure 5.8a. (b) Model M of the artefacts in (a).

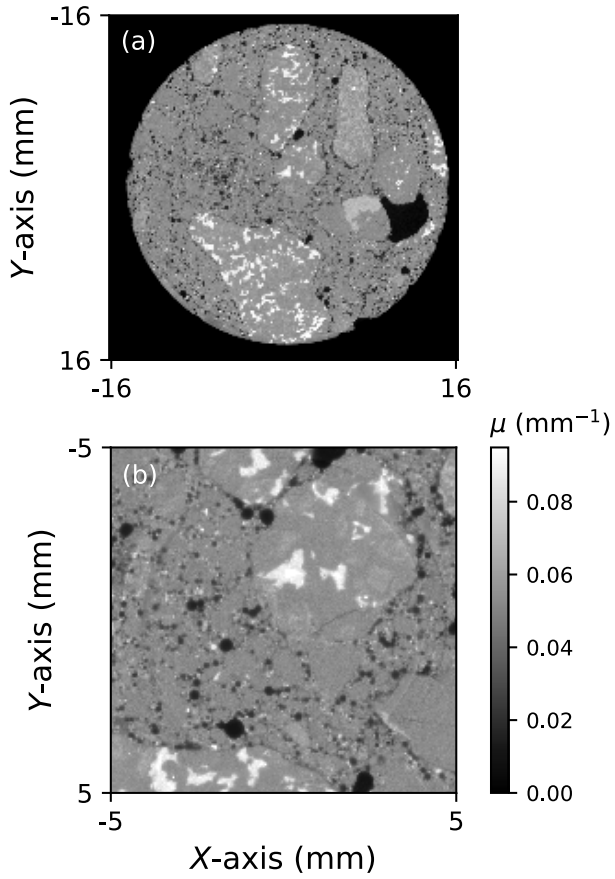

Figure 5.10: Reconstruction of the slice of the concrete rod by DIRECTT in two different magnifications.

Table 5.2: The *mean squared error* (MSE) and the *structural similarity index metric* (SSIM) of the slices in Figures 5.8b and 5.10 in reference to the corresponding slice of the volumes in Figure 5.5 that were reconstructed by FDK and DIRECTT.

Algorithm	Reference in Fig. 5.5:	MSE ($\times 10^{-4}$ mm^{-2}) FDK	MSE ($\times 10^{-4}$ mm^{-2}) DIRECTT	SSIM FDK	SSIM DIRECTT
FDK (Fig. 5.8b)		3.8	3.8	0.83	0.80
DIRECTT (Fig. 5.10)		0.17	0.06	0.87	0.95

is visible at this scale. A (10 mm)^2-region around the centre of the same slice is shown in magnification in Figure 5.10b. There is only a slight gradient around the pixels that correspond to the ring artefact in Figure 5.8b. The MSE of the slice in reference to the corresponding slice of the volume that was reconstructed by FDK in Figure 5.5 is 1.7×10^{-5} mm^{-2}; its SSIM is 0.87. The corresponding slice of the volume that was reconstructed by DIRECTT in Figure 5.5 has a MSE equal 6×10^{-6} mm^{-2} and a SSIM equal to 0.95. These values, along with those for the slice in Figure 5.8b are also compiled in Table 5.2.

Since the ring artefact has been artificially introduced in the presented example, it is known which pixels should be discarded from the sinogram. This does not preclude the implementation of the same approach on real data. Of course, the said implementation would require the identification of the detector pixels to which similar artefacts would be attributed. The pixels would be identified easily based on outlier values in the flat-field image [50].

5.2.2 Region-of-interest measurement

During the measurement of the concrete rod at half its original distance from the source, only a region of interest (ROI) in the shape of cylinder with a diameter of 16.2 mm and a height of 11.8 mm lay fully within the FoV. Cross sections through the volume that was reconstructed by FDK from the acquired projections are shown in the upper row of Figure 5.11. Filtering the truncated projections leads to the artefacts in the form of extremely high μ values tangentially to the ROI [43]. In order to achieve better visualization inside the ROI, the maximum greyscale value was set to 0.1 mm^{-1} causing a "halo" effect in the images.

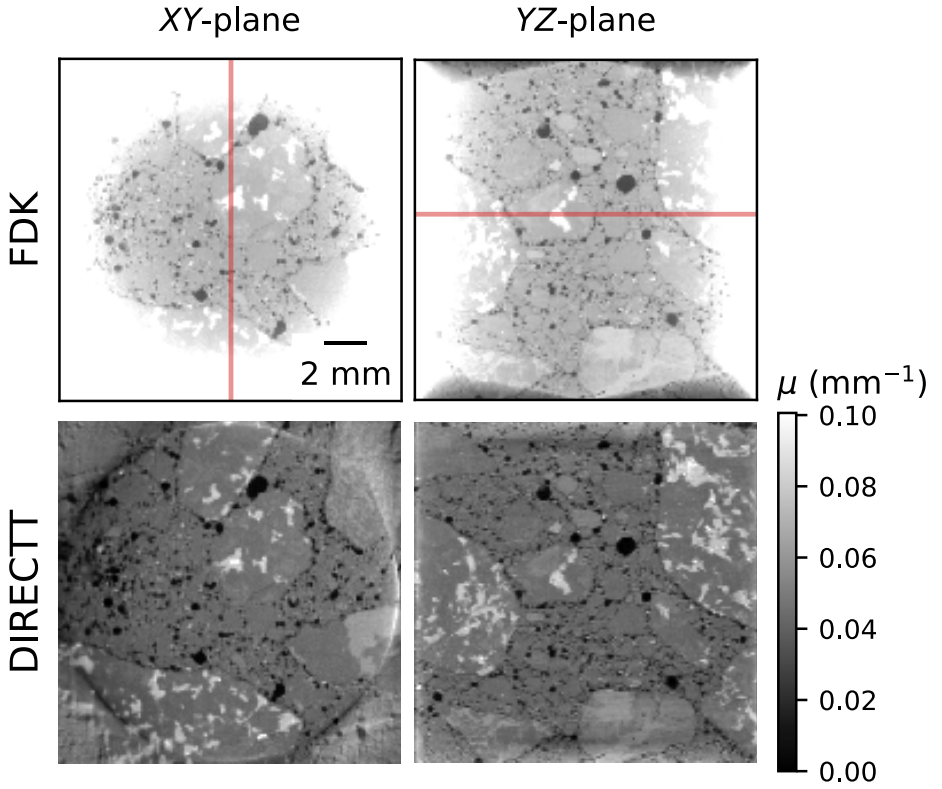

Figure 5.11: Common cross sections through the volumes of the concrete rod that were reconstructed by FDK and DIRECTT from the region-of-interest projections. In order to achieve better visualization inside the ROI in the volume that was reconstructed by FDK, the maximum greyscale value was set to 0.1 mm^{-1} causing a "halo" effect in the images. The red lines in the upper row indicate the relative position of the two cross sections to one another.

Based on the detector voxel size of 0.2 mm and the magnification of 25×, a reconstruction volume of $(16.2\ \text{mm})^3$ was selected for the implementation of FDK. However, in the case of the iterative algorithms, the reconstruction volume must contain the majority of the elements that lay, even partially, within the FoV. This is essential because of the repeated forward- and back-projection operations. Therefore, for the implementation of the iterative algorithms, the volume was expanded to $19.4\times32.4\times32.4\ \text{mm}^3$.

The model M, which is required for the implementation of DIRECTT (Equation 2.4), was computed based on a virtual cylinder C that was inscribed inside the expanded reconstruction volume. The value of α was set to 2.5. Cross sections through the ROI as this was reconstructed by DI-

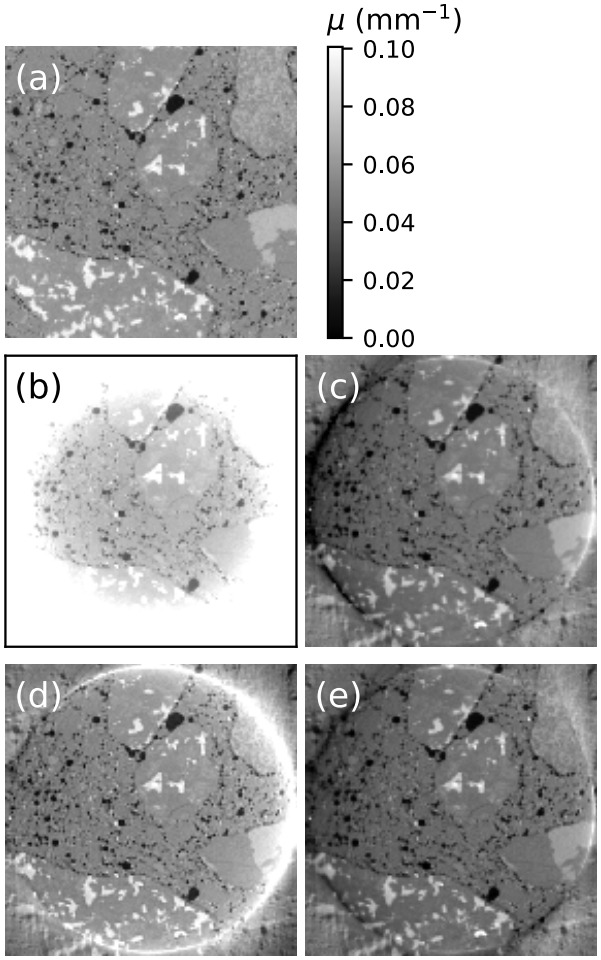

Figure 5.12: (a) The region of interest (ROI) as reconstructed by FDK from the full-width projections and the same ROI as reconstructed by (b) FDK, (c) SIRT, (d) CGLS, and (e) DIRECTT from the truncated projections.

Table 5.3: The *mean squared error* (MSE) and *structural similarity index metric* (SSIM) of each volume in Figures 5.12b-e in reference to the volume in Figure 5.5 that was reconstructed by FDK.

Algorithm	MSE ($\times 10^{-4}\,\mathrm{mm}^{-2}$)	SSIM
FDK	11.5	0.70
SIRT	1.8	0.81
CGLS	2.5	0.78
DIRECTT	1.7	0.80

RECTT are shown in the lower row of Figure 5.11. The area around the edges of the ROI is now mostly devoid of severe artefacts. While the images remain slightly blurred near their corners, they are vastly improved compared to those reconstructed by FDK.

Since both full-width and region-of-interest projections of the same sample have been used in this chapter, the volumes that were reconstructed from the former could be used as the reference for the assessment of the volumes that were reconstructed from the latter. However, this would be possible only if the volume that was assessed had a voxel size that was equal to that of the reference. By taking full advantage of the increased magnification of the ROI measurement, the reconstructed volume would have a voxel size of 8 μm ($2424 \times 4048 \times 4048$ array). Instead, the algorithms were programmed to reconstruct volumes with a voxel size of 16 μm ($1212 \times 2024 \times 2024$ array), using the original projections.

The XY-slices from Figure 5.11 are shown again in Figure 5.12 alongside the corresponding slices from the ROI as reconstructed by SIRT and CGLS. The 16.2×16.2 mm^2 part around the centre of the corresponding slice from the volume that was reconstructed by FDK from the full-width projections is also shown in Figure 5.12a. SIRT performed 800 iterations, CGLS performed 200, and DIRECTT performed 600. Interestingly, compared to FDK, SIRT and CGLS each performed better at suppressing the artefacts on opposite sides of their respective volumes: SIRT on the right side, and CGLS on the left side. On the contrary, DIRECTT performed well at suppressing the artefacts on both sides.

The MSE and SSIM of each volume in Figures 5.12b-e are listed in Table 5.3. A region of dimensions (16.2 mm)^3 around the centre of the volume that was reconstructed by FDK from the full-width projections (Figure 5.5) was used as the reference. The same reference was used for the calculation of the metrics in Figure 5.7. The values of the metrics in Table 5.3 indicate that the volumes that were reconstructed by SIRT and DIRECTT are of similar quality, higher than that of the volume reconstructed by CGLS and much better than that of the volume reconstructed by FDK.

Summary and outlook

This dissertation has dealt with the subject of image reconstruction from Computed Tomography (CT) data. It has specifically focused on the use of iterative algorithms for the reconstruction from under-sampled data.

An overview of the basics of image reconstruction has been given, beginning with the simplest case of a two-dimensional (2D) measurement with a parallel X-ray beam, and extending to three dimensions (3D) and the more complex projection geometry involving a cone beam. This overview included an introduction to the standard *filtered back-projection* (FBP) algorithm, as well as the algorithm developed by Feldkamp, Davis and Kress (FDK) specifically for the reconstruction from cone-beam data. It also introduced the concept of iterative reconstruction, with special reference to two established and easily accessible algebraic-reconstruction algorithms: the *Simultaneous Iterative Reconstruction Technique* (SIRT) and the *Conjugate Gradient Least Squares* (CGLS).

Within the wide subject of image reconstruction, the overarching objective of the dissertation has been the development of the *Direct Iterative Reconstruction of Computed Tomography Trajectories* (DIRECTT) algorithm. DIRECTT was originally proposed by Lange and Hentschel. While it had already been shown to be a promising alternative to FBP algorithms, its implementations was hindered by certain weaknesses. The main weaknesses have been identified here as the repeated and computationally expensive filtering of the projections and the relatively arbitrary selection of elements of the reconstruction array, the values of which would be updated during each iteration. They both affect the efficiency of the algorithm in terms of speed and reconstruction quality.

To overcome these weaknesses, a novel approach to DIRECTT has been proposed. First, the measured (or, after the initial iteration, residual) data are not filtered any more before they are back-projected. Second, a virtual uniform object C of dimensions sufficiently similar to those of the measured object is defined. The relation between the Radon transform of C, which is computed only once, and the measured data is used to easily identify which elements of the reconstruction array will have their values updated during each iteration.

The novel approach to DIRECTT has also been expanded to its im-

plementation for 3D geometries, including acquisitions with a cone-beam. In this particular case, the object C serves a second role. After the Radon transform of the virtual uniform object is computed, as explained above, the result is back-projected to compute the model M. This is a model of artefacts that arise during the back-projection of the data and, even though it needs to be computed only once, it is used to correct the volume prior to the identification of the voxels that will have their values updated during each iteration. Without these corrections, DIRECTT could not be implemented efficiently for cone-beam geometries.

The newly formulated version of DIRECTT has been tested on several datasets that were acquired in both parallel- and cone-beam measurements. Its results have been compared to those of other established algorithms. The evaluation of the results has been performed using an array of full-reference, as well as no-reference metrics.

Regarding the reconstruction from parallel-beam data, the algorithms have been compared for two sets that present different challenges. In the first case, the iterative algorithms have clearly performed better than FBP in suppressing the noise while reconstructing a metal matrix composite cylindrical sample from noisy data. After the introduction of an extra degree of difficulty, through the simulation of a missing-wedge measurement, DIRECTT has been shown to suppress the distortion of the shape of the sample. Hence, it has returned an image that resembles more closely, compared to the other algorithms, the image that is reconstructed from the full dataset. In a second example, a significant number of projections have been deemed unusable because of the large aspect ratio of the scanned grid, resulting in a different, but relevant, case of a missing-wedge measurent. DIRECTT has been shown to perform better, in terms of locating the attenuation coefficient values accurately throughout the reconstruction volume and, consequently, preserving the shape of the apertures of the grid.

Two sets of measured data have been used to compare the reconstruction algorithms for the case of cone-beam CT as well. The sets correspond to different measurements of a concrete sample. In the first case of a conventional, full-width measurement of the sample, the iterative algorithms have performed better than FDK in suppressing artefacts that are associated with the cone-beam geometry. Following the progressive removal of projections from the data, in order to simulate sparse-sampling measurement, DIRECTT has been shown to reconstruct volumes that resemble more closely those that have been reconstructed from the full dataset, compared to the other algorithms. In the second case of a region-of-interest measurement, the iterative algorithms have suppressed the very severe artefacts that arise when reconstructing by FDK.

To sum up, the performance of different reconstruction algorithms has been tested for several distinct cases of CT measurements. Regarding DIRECTT in particular, the novel approach to the reconstruction principle of

the algorithm, which has been presented here, has led to higher efficiency and improved computational time compared to the original version. DIRECTT has been shown to perform the reconstruction from any dataset at least as well as other algorithms. In fact, in most cases, DIRECTT outperforms them. The number of iterations that DIRECTT requires is practical, even if typically larger that that of CGLS. It is comparable to the number of iterations required by SIRT and often even smaller.

There is definitely a potential for further improvement of DIRECTT. Future work will mostly focus on the modelling of the scanned object. A fast but accurate estimation of the shape and geometry will improve further the efficiency of the algorithm in terms of speed and reconstruction quality. For instance, different artefacts, e.g. metal artefacts, could be suppressed if the factors that cause them are included when the object C and/or the model M are defined. In addition, the relative simplicity of the mathematical concepts that the iterative of DIRECTT is based on means that higher-level programming could reduce the required running time of the algorithm by several degrees.

Bibliography

[1] A. M. Al-Falahat, A. Kupsch, M. P. Hentschel, A. Lange, N. Kardjilov, H. Markötter, and I. Manke. Correction approach of detector backlighting in radiography. *Review of Scientific Instruments*, 90(12):125108, 2019.

[2] S. Allner, A. Gustschin, A. Fehringer, P. B. Noël, and F. Pfeiffer. Metric-guided regularisation parameter selection for statistical iterative reconstruction in computed tomography. *Scientific Reports*, 9(1):6016, 2019.

[3] C. Axelsson and P. Danielsson. Three-dimensional reconstruction from cone-beam data in $O(N^3 \log N)$ time. *Physics in Medicine and Biology*, 39(3):477–491, 1994.

[4] M. Bartscher, U. Hilpert, and D. Fiedler. Ermittlung der Messunsicherheit von Computertomographie-Messungen am Beispiel eines Zylinderkopfs (Determination of the Measurement Uncertainty of Computed Tomography Measurements Using a Cylinder Head as an Example). *tm - Technisches Messen*, 75(3):178–186, 2008.

[5] M. Beister, D. Kolditz, and W. A. Kalender. Iterative reconstruction methods in X-ray CT. *Physica Medica*, 28(2):94–108, 2012.

[6] M. Boin and A. Haibel. Compensation of ring artefacts in synchrotron tomographic images. *Optics Express*, 14(25):12071–12075, 2006.

[7] R. A. Brooks and G. D. Chiro. Principles of computer assisted tomography (CAT) in radiographic and radioisotopic imaging. *Physics in Medicine and Biology*, 21(5):689–732, 1976.

[8] O. Brunke, J. Lübbehüsen, F. Hansen, and F. F. Butz. A new Concept for High-Speed atline and inlineCT for up to 100% Mass Production Process Control. *International Congress of Metrology*, 2013.

[9] S. Cabeza, T. Mishurova, G. Garcés, I. Sevostianov, G. Requena, and G. Bruno. Stress-induced damage evolution in cast $AlSi_{12}CuMgNi$ alloy with one- and two-ceramic reinforcements. *Journal of Materials Science*, 52(17):10198–10216, 2017.

[10] S. Carmignato. Accuracy of industrial computed tomography measurements: Experimental results from an international comparison. *CIRP Annals*, 61(1):491–494, 2012.

[11] CORDIS - EU research Results. Multiscale, multimodal and multidimensional imaging for engineering. https://cordis.europa.eu/project/id/765604/results.

[12] A. M. Cormack. Representation of a function by its line integrals, with some radiological applications. *Journal of Applied Physics*, 34(9):2722–2727, 1963.

[13] L. De Chiffre, S. Carmignato, J. P. Kruth, R. Schmitt, and A. Weckenmann. Industrial applications of computed tomography. *CIRP Annals*, 63(2):655–677, 2014.

[14] L. A. Feldkamp, L. C. Davis, and J. W. Kress. Practical cone-beam algorithm. *J. Opt. Soc. Am. A*, 1(6):612–619, Jun 1984.

[15] P. Gilbert. Iterative methods for the three-dimensional reconstruction of an object from projections. *Journal of Theoretical Biology*, 36(1):105–117, 1972.

[16] W. B. Gilboy. X- and γ-ray tomography in NDE applications. *Nuclear Instruments and Methods in Physics Research*, 221(1):193–200, 1984.

[17] R. Gordon, R. Bender, and G. T. Herman. Algebraic Reconstruction Techniques (ART) for three-dimensional electron microscopy and X-ray photography. *Journal of Theoretical Biology*, 29(3):471–481, 1970.

[18] M. Grass, T. Köhler, and R. Proksa. 3D cone-beam CT reconstruction for circular trajectories. *Physics in Medicine and Biology*, 45(2):329–347, 1999.

[19] J. Gregor and T. Benson. Computational analysis and improvement of sirt. *IEEE Transactions on Medical Imaging*, 27(7):918–924, 2008.

[20] H. Gu, L. Yu, and Y. Wang. CT number in wood physical properties prediction based on computed tomography technology. In *2010 IEEE International Conference on Automation and Logistics*, pages 279–284, Hong Kong, 2010. Institute of Electrical and Electronics Engineers.

[21] L. Györfi and E. C. van der Meulen. Density-free convergence properties of various estimators of entropy. *Computational Statistics & Data Analysis*, 5(4):425–436, 1987.

[22] M. P. Hentschel, A. Lange, A. Kupsch, and B. R. Müller. Rekonstruktion unvollständiger computertomografischer Modelldatensätze mit Directt- Algorithmus. *Materials Testing*, 52(10):668–675, 2010.

[23] M. Hestenes and E. Stiefel. Methods of conjugate gradients for solving linear systems. *Journal of research of the National Bureau of Standards*, 49:409–435, 1952.

[24] G. N. Hounsfield. Computerized transverse axial scanning (tomography): Part 1. description of system. *The British Journal of Radiology*, 46(552):1016–1022, 1973.

[25] S. Kruschwitz, T. Oesch, F. Mielentz, D. Meinel, and P. Spyridis. Nondestructive multi-method assessment of steel fiber orientation in concrete. *Applied Sciences*, 12(2), 2022.

[26] J. P. Kruth, M. Bartscher, S. Carmignato, R. Schmitt, L. De Chiffre, and A. Weckenmann. Computed tomography for dimensional metrology. *CIRP Annals*, 60(2):821–842, 2011.

[27] A. Kupsch, A. Lange, and M. P. Hentschel. Enhanced spatial resolution in 2D CT-reconstruction without Filtered Back Projection: DIRECTT. In *17th World Conference on Non-Destructive Testing (Proceedings)*, pages 643–648, Shanghai, 2008. International Committee for Non-Destructive Testing.

[28] A. Kupsch, A. Lange, M. P. Hentschel, S. Lück, V. Schmidt, R. Grothausmann, A. Hilger, and I. Manke. Missing wedge computed tomography by iterative algorithm DIRECTT. *Journal of Microscopy*, 261(1):36–45, 2016.

[29] A. Kupsch, A. Lange, M. P. Hentschel, and B. R. Müller. Improved Computed Tomography by Variable Desmearing: Model Reconstructions by Iterative DIRECTT Algorithm. *Materials Testing*, 52(6):394–400, 2010.

[30] A. Kupsch, A. Lange, M. P. Hentschel, Y. Onel, T. Wolk, A. Staude, K. Ehrig, B. R. Müller, and G. Bruno. Evaluating porosity in cordierite diesel particulate filter materials, part 1: X-ray refraction. *Journal of ceramic science and technology*, 4(4):169–176, 2013.

[31] A. Lange and M. P. Hentschel. *Bildgebendes Verfahren und Vorrichtung zur rechnergestützten Auswertung computertomographischer Messungen durch direkte iterative Rekonstruktion.* Patent No. DE 103 07 331 Q4 A1, Germany, 2003.

[32] A. Lange and M. P. Hentschel. *Imaging method and device for the computer-assisted evaluation of computer-tomographic measurements by means of direct iterative reconstruction.* Patent No. US 2006 0233459 A1, United States of America, 2006.

[33] A. Lange, M. P. Hentschel, and A. Kupsch. Computertomographische Rekonstruktion mit DIRECTT: 2D-Modellrechnungen im Vergleich zur gefilterten Rückprojektion. *Materials Testing*, 50(5):272–277, 2008.

[34] A. Lange, M. P. Hentschel, and A. Kupsch. True 3D-CT-reconstruction in comparison to the FDK-algorithm. In *17th World Conference on Non-Destructive Testing (Proceedings)*, pages 491–495, Shanghai, 2008. International Committee for Non-Destructive Testing.

[35] A. Lange, A. Kupsch, M. P. Hentschel, I. Manke, N. Kardjilov, T. Arlt, and R. Grothausmann. Reconstruction of limited computed tomography data of fuel cell components using Direct Iterative Reconstruction of Computed Tomography Trajectories. *Journal of Power Sources*, 196(12):5293–5298, 2011.

[36] S. Lück, A. Kupsch, A. Lange, M. P. Hentschel, and V. Schmidt. Statistical analysis of tomographic reconstruction algorithms by morphological image characteristics. *Image Analysis & Stereology*, 29(2), 2011.

[37] S. Magkos. Graphic User Interface for reconstruction from Computed Tomography data. https://github.com/BAMresearch/DIRECTT, 2021.

[38] S. Magkos, A. Kupsch, and G. Bruno. Direct Iterative Reconstruction of Computed Tomography Trajectories Reconstruction from limited number of projections with DIRECTT. *Review of Scientific Instruments*, 91(10):103107, 2020.

[39] S. Magkos, A. Kupsch, and G. Bruno. Suppression of Cone-Beam Artefacts with Direct Iterative Reconstruction Computed Tomography Trajectories (DIRECTT). *Journal of Imaging*, 7(8):147, 2021.

[40] Mathworks. Image quality metrics. https://www.mathworks.com/help/images/image-quality-metrics.html.

[41] A. Mittal, A. K. Moorthy, and A. C. Bovik. Blind/Referenceless Image Spatial Quality evaluator. In *2011 Conference Record of the Forty Fifth Asilomar Conference on Signals, Systems and Computers (ASILOMAR)*, pages 723–727, Pacific Grove, California, 2011.

[42] A. Mittal, R. Soundararajan, and A. C. Bovik. Making a "completely blind" image quality analyzer. *IEEE Signal Processing Letters*, 20(3):209–212, 2013.

[43] M. Müller and G. R. Arce. Truncation artifacts in tomographic reconstructions from projections. *Applied Optics*, 35(20):3902–3914, 1996.

[44] Nobel Foundation. The nobel prize in physiology or medicine 1979. https://www.nobelprize.org/prizes/medicine/1979/summary.

[45] A. Rack, S. Zabler, B. R. Müller, H. Riesemeier, G. Weidemann, A. Lange, J. Goebbels, M. Hentschel, and W. Görner. High resolution synchrotron-based radiography and tomography using hard X-rays at the BAMline (BESSY II). *Nuclear Instruments and Methods in Physics Research Section A: Accelerators, Spectrometers, Detectors and Associated Equipment*, 586(2):327–344, 2008.

[46] R. Reams. Hadamard inverses, square roots and products of almost semidefinite matrices. *Linear Algebra and its Applications*, 288:35–43, 1999.

[47] P. Reimers, J. Goebbels, H. P. Weise, and K. Wilding. Some aspects of industrial non-destructive evaluation by X- and γ-ray computed tomography. *Nuclear Instruments and Methods in Physics Research*, 221(1):201–206, 1984.

[48] J. L. Rodgers and W. A. Nicewander. Thirteen ways to look at the correlation coefficient. *The American Statistician*, 42(1):59–66, 1988.

[49] D. Schob, I. Sagradov, R. Roszak, H. Sparr, R. Franke, M. Ziegenhorn, A. Kupsch, F. Léonard, B. R. Müller, and G. Bruno. Experimental determination and numerical simulation of material and damage behaviour of 3D printed polyamide 12 under cyclic loading. *Engineering Fracture Mechanics*, 229:106841, 2020.

[50] J. A. Seibert, J. M. Boone, and K. K. Lindfors. Flat-field correction technique for digital detectors. In *Medical Imaging 1998: Physics of Medical Imaging*, volume 3336, pages 348–354, San Diego, 1998. SPIE.

[51] L. A. Shepp and B. F. Logan. The Fourier reconstruction of a head section. *IEEE Transactions on Nuclear Science*, 21(3):21–43, 1974.

[52] J. Sijbers and A. Postnov. Reduction of ring artefacts in high resolution micro-CT reconstructions. *Physics in Medicine and Biology*, 49(14):N247–N253, 2004.

[53] O. Taubmann, M. Berger, M. Bögel, Y. Xia, M. Balda, and A. Maier. *Computed Tomography*, pages 147–189. Springer International Publishing, Cham, 2018.

[54] W. Technologies. Industrial computed tomography innovations, 2020.

[55] H. K. Tuy. An inversion formula for cone-beam reconstruction. *Siam Journal on Applied Mathematics*, 43:546–552, 1983.

[56] W. van Aarle, W. J. Palenstijn, J. Cant, E. Janssens, F. Bleichrodt, A. Dabravolski, J. De Beenhouwer, K. Joost Batenburg, and J. Sijbers. Fast and flexible X-ray tomography using the ASTRA toolbox. *Optics Express*, 24(22):25129–25147, 2016.

[57] N. Venkatanath, D. Praneeth, B. Maruthi Chandrasekha, S. S. Channappayya, and S. S. Medasani. Blind image quality evaluation using perception based features. In *2015 Twenty First National Conference on Communications*, pages 1–6, Mumbai, 2015.

[58] Z. Wang and A. C. Bovik. Mean squared error: Love it or leave it? A new look at Signal Fidelity Measures. *IEEE Signal Processing Magazine*, 26(1):98–117, 2009.

[59] Z. Wang, A. C. Bovik, H. R. Sheikh, and E. P. Simoncelli. Image quality assessment: from error visibility to structural similarity. *IEEE Transactions on Image Processing*, 13(4):600–612, 2004.

[60] G. L. Zeng. Image reconstruction — a tutorial. *Computerized Medical Imaging and Graphics*, 25(2):97–103, 2001.

[61] G. L. Zeng. A Skew-Slit Collimator for Small-Animal SPECT. *Journal of Nuclear Medicine Technology*, 36(4):207, 2008.

[62] G. L. Zeng. *Image Reconstruction: Applications in Medical Sciences*. De Gruyter, Berlin, 2017.